University of Nevada, Reno

Hydrochemical Response of Groundwater Following the 2020 Monte Cristo Range Earthquake Sequence within Mineral and Esmeralda Counties, NV

A thesis submitted in partial fulfillment of the requirements for the degree of Master of Science in Hydrogeology

By

Dylan K. Morlang

Dr. Paula J. Noble/Thesis Advisor

August 2022

THE GRADUATE SCHOOL

We recommend that the thesis
prepared under our supervision by

Dylan K. Morlang

entitled

Hydrochemical Response of Groundwater Following the 2020 Monte Cristo Range Earthquake Sequence within Mineral and Esmeralda Counties, NV

be accepted in partial fulfillment of the
requirements for the degree of

MASTER OF SCIENCE

Paula J. Noble, Ph.D.
Advisor

Simon R. Poulson, Ph.D.
Committee Member

William C. Hammond, Ph.D.
Graduate School Representative

Markus Kemmelmeier, Ph.D., Dean
Graduate School

August, 2022

Abstract

The 2020 Monte Cristo Earthquake sequence in western Nevada began with a M 6.5 shock on 5/15/2020, and was the largest to occur in Nevada since 1954. The event exhibited left-lateral slip along an eastward extension of the Candelaria fault and extensive distributed surface faulting in the epicentral area. Groundwater monitoring and strain analysis were conducted to evaluate hydrochemical effects on the regional groundwater systems following the introduction of both static and dynamic strain. Physiochemical monitoring, began on 5/16/2020 and included measurements of temperature (temp), pH, specific conductance (SpC), flow rate, alkalinity and collection of samples for isotopic and elemental analysis. Since sites had not been monitored prior to the initial shock, measurements were evaluated against a year of post-event data to gauge response to seismicity. Four sites were monitored: a well from Columbus Marsh (CM) located 5 km from the epicenter; an artesian thermal well from Fish Lake Valley (FLV); a well at Willow Ranch (WR) tapping cool water above the FLV waters; and a spring along Mina Dump Road (MD) located 15 km north of the Candelaria fault on the Benton Springs Fault. GPS and InSAR measurements were used to create a model of the slip of the M 6.5 event, from which coseismic static strain was calculated at each sampling location. All but one sample site, MD, experienced positive dilatation and CM experienced the greatest amount of static strain (1.2E6 nanostrains). Hydrologic and chemical changes were observed following the initial shock and aftershocks >M 4, varying between sites and event. CM had significantly lower SpC values in the week following the May 15th event. During the early part of the seismic series, a period of high frequency and intensity aftershocks, MD showed a suppressed flow rate. Several aftershock sequences that were host to >M 4 events were also modeled in an elastic half

space to estimate coseismic static strain as a result of less intense earthquakes. Clear physiochemical responses were observed throughout three aftershock sequences (6/30/2020, 11/13/2020, and 12/2/2020) and show a high correlation to the sign and magnitude of strain each site experienced. The clearest of these responses were recorded as a result of the 11/13/2020 and 12/2/2020 aftershock sequences. Between these two events, differential stress correlated well with the differential response seen as an increase in the temp of CM and WR trending with an increase in stress at these sites leading up to 11/13/2020. SpC dropped at CM and FLV and pH at CM after dilatational strain was modeled at both sites as a result of the 11/13/2020 event. The trend in SpC and pH at CM was reversed following contractional static strain the site on 12/2/2020. The trend in FLV also reversed on 12/2/2020, but instead, due to the location of dilatational static strain relative to the site. This study provides the framework of a new method to better analyze the impacts earthquakes have on the hydrogeological environment. Elemental chemical analysis is planned to further the understanding of earthquake mechanisms and their response in the Basin and Range.

Acknowledgements

I would like to express my deepest gratitude to my advisor Dr. Paula Noble for her invaluable assistance and patience. Also, this endeavor would not have been possible without the input from my committee, Dr. William Hammond, and Dr. Simon Poulson. I'm extremely grateful for Dr. Lisa Stillings and Dr. Michael Rosen for their part in providing vital assistance throughout this project. Additionally, thanks should go to the National Science Foundation for their generous support in funding my research.

I am deeply indebted to my colleagues at the Università dell'Insubria including Dr. Gilberto Binda, Andrea Pozzi, and Alessandro Michetti for their part in offering their expert input in the analysis of data as well as their selfless offer to process samples and further this project.

I am also grateful to my classmates and officemates for their support along this journey, particularly Gary McGaughey for his help in not only providing edits, but also his assistance in collecting data.

This project would not be possible without the help of Forrest and Nadine Fasig who selflessly offered their knowledge of the research area and volunteered their time to collect data during the most crucial moments of this research.

I would like to extend my sincere thanks to both Adam Chiparro as well as the management of Ireland Minerals for allowing us access to their wells for sampling.

Special thanks to John Gansfuss for providing professional guidance while reviewing my writing.

Lastly, I would be remiss in not mentioning my family for their persistent motivation and support during this process.

Dylan Morlang

Table of Contents

Tables

Figures

Appendices

1. Introduction

It has been known that seismic activity has a direct impact on the surrounding groundwater systems. Changes in water level, discharge, groundwater contours, and chemistry have been previously observed in response to seismic activity (Binda et al., 2020; Brodsky, 2003; Manga & Wang, 2015). However; understanding the mechanisms driving these groundwater responses, and the specific ties to tectonic forces is a subject needing further study. Here, seismic intensity and tectonic strain is analyzed in conjunction with physiochemical changes in groundwater at localities in close proximity (~40km radius) to the Monte Cristo seismic sequence. This sequence began on May 15th, 2020 with a M 6.5 earthquake within the Monte Cristo Range and was followed by thousands of aftershocks and several >M_w 5 events that occurred in late June, November, and December 2020 (Figures 1 & 2).

A hydrochemical monitoring program was established by Dr. Paula Noble of the University of Nevada, Reno the day after the initial Monte Cristo event. Monitoring occurred at four principal sites within a ~30 km radius of the M 6.5 epicenter, and continued through December 2021 (Tables 1 & 2). This distance roughly corresponds to the VI intensity isoseismal line on the Modified Mercalli intensity scale (MMI) from the initial shock (Figure 2), a distance that had been determined in previous studies to be within the range of groundwater sensitivity (Binda et al., 2020). Continuous monitoring of these locations provides interesting comparisons of differential responses between sites that are located in varied settings spanning three hydrographic basins and on both North and South sides of the fault (Figure 2).

Renewed seismicity over the six months following the main shock showed notable effects in the region, with aftershocks and cumulative seismic moment (Mo)

continuing throughout May, followed by bursts of energy released in June, November, and December 2020 (Figure 3). By 2021 aftershock intensity decayed. Although not exceeding M_w 5.3, the 18-month interval beginning with the main shock provides a useful time series with both pre- and post-seismic data with which to evaluate groundwater response. When referencing times of increased seismic activity, periods of interest are identified by the date of the largest earthquake that took place within that time period. Modeling of these sequences was conducted on seismicity > M_w 4 that took place within two days of the date of the largest earthquake in the period. In the days surrounding the June 30th aftershocks there were around 80 earthquakes per day and one M_w 5 shock. There were around 100 earthquakes per day, two of which were > M_w 4 and one was > M_w 5 as a part of the November 13th aftershocks. Around 135 earthquakes per day took place during the December aftershocks, six of them were > M_w 4 and one was > M_w 5.

The broader impacts of this study pertain to the health and safety rural Nevadans who rely heavily on groundwater, with many municipalities using wells as their sole public source. Around the study area, local communities include Hawthorne and Tonopah. Understanding the effects of seismicity on this important resource will be of value in maintaining and protecting groundwater in the future.

A. Previous Studies

There have been numerous papers published outlining the changes in groundwater associated with seismic activity across the world. Primary effects of seismic activity include hydrogeochemical anomalies, change in flow rates, and change in water levels. Hydrogeochemical response in groundwater as a result of seismic events have been discussed in several papers, synthesizing studies spanning across 30 years of data collection and analysis with extensive work in the Apennines Mountains in Italy

(Binda et al., 2020, Rosen et al., 2018), as well as other regions including Japan, Alaska, Taiwan, California, and New Zealand (Manga and Wang, 2015). Some studies help characterize the mechanisms that affect chemical changes in groundwater (Binda et al. 2020, Rosen et al. 2018, Brodsky et al. 2003). Specifically, poroelastic response is attributed to changes in static strain, either dilatational or contractional which is considered a significant co-seismic driver in groundwater chemistry (Manga and Wang, 2015). Pore pressure changes were suggested to cause expulsion of high solute-rich pore water in karstic aquifers in the Apennines of Italy, resulting in transient increases in conductivity and ion concentrations (Rosen et al., 2018; Binda et al., 2020).

Several studies have been published in the last 20-30 years focusing on deviations in groundwater flow both leading up to and following major earthquakes. These studies found that sudden changes in groundwater flow have been attributed to increased strain, resulting in a modification of groundwater pressure gradients and groundwater topography (Manga and Wang, 2015). Other changes in flow have been attributed to dynamic strain as a result of shaking, which can either increase flow rates though breaking up precipitates within flow paths (Brodsky et al., 2002), or decrease flow rates by clogging pore spaces from particulate matter in turbid groundwater (Manga and Wang, 2015).

Precursory signals of seismicity are particularly important in the effort to accurately forecast future seismic hazards. A review of precursory groundwater observations over the past 1400 years was developed by Martinelli et al (2020), and several tentative precursory signals such as the release of gasses (CO_2) and several elements (As, V, Cr, and Fe) were interpreted in a few localities following the 2016 central Italy seismic sequence (Barbiero et al., 2017). However, precursory signs to seismic activity, while well documented after seismic events, appear to be inconsistent

between events, localities, and remain elusive (Binda et al., 2020).

The majority of conclusions from previous studies related to groundwater response as a result of seismicity highlight that groundwater response is often localized, and may vary between events. In fact, some data can appear contradictory, likely as a result of varying mechanisms driving different groundwater responses. In some cases, distance from epicenter is not always proportional to the size of the response (Binda et al, 2020), calling into the question the importance of local subsurface geology, and crustal response to tectonic stresses.

B. Stress and Its Impact on Groundwater Systems

As discussed by Manga and Wang (2015) both dynamic and static stresses produced during seismic events can evoke hydrologic response. Dynamic stress, caused by the propagation of seismic waves, is proportional to the magnitude (surface wave amplitude) of the event, and the effects are spatially variable based on the propagation patterns and attenuation of these waves. Static stresses are introduced onto earth's crust as a result of the displacement of a fault. With the introduction of both dynamic and static stresses, porous media experience dynamic and static strains and concomitant changes in pore pressure. The result is poroelastic deformation, which plays a direct role in changes in water levels and flow within groundwater systems. The intensity and therefore the amount of stress dynamic waves induce doesn't decay as fast as those associated with static stress and as a result, dynamic stresses can be significant even in the far field (Lay & Wallace, 1995; Manga & Wang, 2015).

The magnitude of static strain will attenuate with distance based on the elasticity of the media. The distribution of static strain deformation is typically modeled using a double-force-couple model in an elastic medium. The deformation could result in additive

or subtractive effects based on the magnitude of strain and location relative to the source (Lay & Wallace, 1995). Also depending on the location of the source, the induced strain may be dilatational or contractional. Therefore, both the magnitude and sign of the strain will have a direct impact on pore pressure in the aquifer and can vary depending on the location of the sample site. Contractional strain may result in increased water levels where dilatational strain may reduce water levels (Manga & Wang, 2015).

Mechanisms determining the behavior of various subsurface media in response to dynamic and static strain are discussed below and used to explain various hydrologic responses over the course of the Monte Cristo Seismic Sequence.

i. Effects of Dynamic Strain

Dynamic strain has been observed to induce several changes in groundwater systems. One change in has been associated with the introduction of new and/or additional contributions of source water, attributed to the process of unclogging fractures per Brodsky et al. (2003). Another may include the consolidation and or agitation of loose sediments in shallow groundwater systems, therefore restricting flow (Manga & Wang, 2015; Fetter, 2018).

Over time, there can be a buildup of weathering products and colloidal material in fractures and faults that can restrict flow. As a result, fractures can act more like aquitards rather than permeable conduits. Seismicity can induce a dynamic wave response in groundwater which acts on these blockages, potentially disturbing particulates or precipitates and increasing flow through these conduits. This process may also cause changes in the hydraulic gradient and may lead to transient changes in flow until hydraulic head has re-equilibrated (Figure 4).

Intrinsic permeability is directly related to the flow rate within a porous medium. When pore diameter changes, it drives exponential changes in flow (Fetter, 2018).

Seismically induced shaking can cause a redistribution of grains, agitating sediment that may clog pore spaces and reduce porosity and permeability. The redistribution of grains in drained or low pore pressure environments can result in consolidation of sediments, a mechanism that would reduce permeability and flow (Figure 5).

ii. Effects of Static Strain

When examining the effects of static strain, dilatation in semi-unconsolidated valley floor material pulls sediment grains apart, increasing pore space and reducing pore pressure. In consolidated rock, static strain can induce fracturing or open-up existing fractures and breach low-permeability barriers which would increase permeability and flow, and also allow for mixing of waters (Fetter, 2018; Lay & Wallace, 1995; Manga & Wang, 2015).

The process of mixing induced by dilatation can be understood using the equations for both the intrinsic permeability and discharge as per Darcy's Law. Increased pore space increase intrinsic permeability as discussed above, and steeper hydraulic gradients result in much faster flow per Darcy's Law (Fetter, 2018). Due to pore pressure gradients water will radially flow toward the dilatational environment and may sink lower in the aquifer while restabilizing hydraulic head (Manga & Wang, 2015). In doing so, waters in a chemically stratified aquifer may undergo vertical mixing in response to the increased vertical component of the hydraulic gradient (Figure 6). A similar response can be seen in chemically stratified aquifers that experience changes in TDS and elemental chemistry as a result of groundwater pumping (Piscopo et al., 2020). According to Darcy's Law, the steeper the hydraulic gradient is, the more "discharge" or flow will be directed toward the site (Fetter, 2018). Therefore, the amount of mixing that takes place in an aquifer may be proportional to the amount of strain.

Contractional or compressional strain tends to have the opposite effect relative to

dilatational strain in groundwater. Contractional strain would increase poroelastic pressure, which could provide a driving force that creates an outward or upward motion of groundwater, as well as over-pressuring and potentially fracturing confining layers (Figure 7). Contractional strain can decrease permeability and reduce flow through a mechanism of closing fractures and decreasing pore spaces in both consolidated and unconsolidated media (Manga & Wang, 2015).

C. Tectonic Significance

From a tectonic standpoint, this sequence is associated with an east-northeast striking fault in the Mina Deflection, a structural anomaly located within the Central Walker Lane in Esmeralda County, Nevada. The Walker Lane is a ~100 km wide diffuse zone of normal and strike-slip faults that extends ~500 kilometers along the Eastern Sierra Nevada, from northern Kern County to southern Modoc County, California, and accommodates ~20% of the dextral lateral shear between the Pacific and North American plates (Pierce et al., 2020). The Walker Lane steps eastward 50 km, entering Nevada at the Mina Deflection. The epicenter of the May 15th, 2020 M 6.5 event took place on an eastern extension of the Candelaria Hills Fault, located within Esmeralda County, Nevada (Figures 1 & 2).

The co-seismic displacements recorded by the MAGNET GPS Network as a result of the May 15th, 2020 Monte Cristo event suggest clockwise block rotation due to left-lateral movement of the east-west trending Candelaria Hills Fault (Hammond et al., 2021; Zheng et al., 2021). This fault plane is near vertical and was modeled to have experienced a total co-seismic slip of ~1 m on May 15th, 2020 (Hammond et al., 2021). The Candelaria Hills Fault is bordered on both sides by northwest-southeast trending faults (Figure 2). To the east are the Benton Springs and the Petrified Springs Faults and

to the west are the White Mountain and Owens Valley Faults (Koehler et al., 2021).

The last major episode of seismicity that took place within the Mina Deflection was in the early 1930's, with the M 7.2 Cedar Mountains and the M 6.3 Excelsior Mountains Earthquakes. These occurred ~40 km NE and ~30 km WNW of the May 15th, 2020 Monte Cristo epicenter, respectively (Figure 2). The Monte Cristo event was one of two major seismic events which bridged a ~400 km gap in seismicity. This gap was present between the 1954 M 7.3 Fairview Peak Earthquake and the 2019 M 7.1 Ridgecrest Earthquake. The other event bridging this gap was 1986 M 6.3 Chalfant Earthquake, 90 km southeast of the Monte Cristo event in Chalfant Valley, California (Figure 1). The May 15th, 2020 Monte Cristo event was the largest seismic event in the state of Nevada since the Fairview Peak event in 1954 (Hammond et al., 2021; Koehler et al., 2021).

D. Monitoring Sites

Each of the four principal sites monitored during this study are described below, including watershed characteristics and hydrogeology. Three of these four sites are wells (the Columbus Marsh, Fish Lake Valley, and Willow Ranch) and two (Mina Dump Road and Fish Lake Valley) have artesian flow.

i. Columbus Marsh

The Columbus Marsh site is positioned at the northern end of a playa valley ~10 km SE of the epicenter of the May 15th, 2020 main shock (Figure 2). Based on the modeled fault length of ~17 km (Hammond et al., 2021) this site is located in the near field. Our definition of near and intermediate field distances from epicenters is consistent with Rosen et al. (2018), where near field is within 1 fault length and intermediate field is within 2-10 fault lengths of the epicenter. This is important to consider when weighing

the effects of seismicity as the intensity of seismicity is largely a matter of distance from the epicenter. The reach of the effects of an earthquake can be attributed to its fault length as generally longer faults host larger shocks.

The Columbus Marsh site is located within the Columbus Valley Hydrographic Basin (basin #118) (Figure 2), a terminal closed basin (Harrill & Prudic, 1998). The sample site is a 16-meter-deep high-flow (0.02 m^3/s) well that produces briny water since the valley is largely a salt marsh. Basin fill has been characterized as having an estimated transmissivity of 310 m^2/d (Maurer et al., 2004; Van Denburgh et al., 1970). Recharge in this basin is partially in the form of runoff (Figure 8A), which contributes an average of 2,400 m^3/d (Van Denburgh et al., 1970). The other source of surficial flow into the valley is an intermittently flowing channel from the south that originates in the Fish Lake Valley Hydrographic Basin (#117). Subsurface flow has been accounted for from the east in the Big Smokey Valley Hydrographic Basin (#137) as well as from the south in the Fish Lake Valley Hydrographic Basin (#117), and totals around 11,000 m^3/d (Lopes & Evetts, 2004; Van Denburgh et al., 1970). Recharge from the west and south interacts predominantly with Miocene and Pliocene consolidated and unconsolidated rhyolitic ash flow bedrock. To the south, recharge also interacts with quartzite and shales containing chert and limestone (Ferguson et al., 1953). This well experienced seismic intensities of VII-VIII the main event (Figures 2 & 9) (*U. S. Geological Survey Earthquakes*, 2020).

ii. Fish Lake Valley Hot Well

The Fish Lake Valley hot well is located in the north eastern section of the Fish Lake Valley Hydrographic Basin (basin #117) (Figures 2 & 10), around 35 km SSW of the epicenter of the initial May 15th, 2020 shock (Harrill & Prudic, 1998). The Fish Lake Valley hot well is considered to be in the intermediate field of the main shock.

This site is significant because it serves as a groundwater source for the Columbus Salt Marsh and represents a deeper groundwater source in the Fish Lake Valley with geothermal influence (Van Denburgh et al., 1970). It is the only well within this study influenced by geothermal activities, likely due to its greater depth relative to other sites, and due to its location within the valley (Figures 2 & 10) (Spurr, 1905). The artesian well flows naturally, under pressure from a confined aquifer. It was one of several Lithium exploration wells drilled in the Fish Lake Valley in the 1970's. Even though this well was initially much deeper than at present (1,525 m), it was grouted up to a depth of 163 m. Initial drilling records reported alluvium to a depth of 1,525 m with "artesian water sands" reported at depths of 177-180 m and 350-457 m (Rush et al., 1973). This hot well produces thermal waters at a rate of ~2 E-4 m^3/s. Estimates of the transmissivity of the aquifers within this basin range between 1,250-2,500 m^2/d. The hydrology of the Fish Lake Valley Hydrographic Basin is shown schematically in figure 9B. Most recharge in the Fish Lake Valley Hydrographic Basin is sourced from mountain runoff, which either seeps into alluvium at the base of the White Mountain Range, or flows across the valley floor through a total of six intermittently flowing streams. These streams all migrate northward towards the hot well where they either evaporate or infiltrate into the sediment. The results of these processes lead to an average annual recharge of around 110,000 m^3/d (Rush et al., 1973). During recharge, waters interact with several geologic rock units. These include Pliocene basalts and quartz ash flows, Eocene conglomerate sedimentary units, Jurassic coarse granites, and Precambrian siltstones. In close proximity to the well, water interacts with young alluvium and rhyolitic ash flows (Albers & Stewart, 1972). The well experienced seismic intensities of V-VI during the main shock (Figure 2) (*U. S. Geological Survey Earthquakes*, 2020).

iii. Willow Ranch

The Willow Ranch is also located in the northern region of the Fish Lake Valley Hydrographic Basin (basin #117), 5km west of the Fish Lake Valley hot well site and 40km SW of the epicenter of the May 15th, 2020 main shock (Harrill & Prudic, 1998) (Figure 2). The Willow Ranch is considered to be in the intermediate field of the initial event.

Unlike the Fish Lake Valley hot well, the Willow Ranch well taps a cold valley-fill reservoir located stratigraphically directly above the aquifer from which the Fish Lake Valley hot well is sourced. The well is ~50 meters deep, and is a residential well. The estimated transmissivity is identical to that of the Fish Lake Valley hot well and is between 1,250-2,500 m^2/d (Rush et al., 1973). Recharge processes and aquifer properties for the Willow Ranch site are slightly different from that of the Fish Lake Valley hot well. Recharge in the basin is sourced from runoff from the White Mountains (Figure 9B), but instead of infiltration occurring at the base of the mountain range, the aquifer this well taps is predominantly recharged by the six intermediate flowing channels originating on the eastern side of the White Mountains (Harrill & Prudic, 1998; Maurer et al., 2004). As these channels flow across the valley floor, water percolates into the soil. This site shares a basin and therefore has the same average basin recharge as the Fish Lake Valley hot well, experiencing an average, 110,000 m^3/d (Rush et al., 1973). Recharge at this site interacts with the same rock units as the hot well, with the exception of the rhyolitic ash flows, which are absent. The well is drilled into younger alluvium, primarily composed of gravel, sand, silt, and clay. Here, seismic intensities of V-VI were experienced during the main shock (Figure 2) (*U. S. Geological Survey Earthquakes*, 2020). During the monitoring interval, the owner reported a well pump failure and deepened the well as he installed a new pump. This occurred in September

2020 (Personal communication from owner of Willow Ranch, Adam Chiparro).

iv. Mina Dump Road Spring

The Mina Dump Road spring is located within the Eastern Soda Spring Hydrographic Basin (basin number 121A), about 40km NNW of the epicenter (Harrill & Prudic, 1998) (Figures 2 & 11). The Mina Dump Road spring is considered to be in the intermediate field of the initial event. This sample location differs from the other three sites monitored in that it is the only site located north of the May 15th, 2020 shock.

The spring is artesian, flowing out of a metal pipe on the south side of the dump road. Recharge (5,400 m^3/d) to this part of the valley is largely from surficial runoff from the surrounding Pilot Mountains. A more direct influence on the flow rate at this site may come from the Southern Pacific Spring, located 1.25 km uphill from the site (Figure 9C). These are shallower groundwater systems than other sites in this study and are expected to have less interaction with regional groundwater, instead having greater influence from local meteorology. Some groundwater flow paths that reach this site may originate higher up within the Pilot Mountains. Other recharge sources include groundwater inflow to the alluvial aquifer (2,000 m^3/d) and a less significant (700 m^3/d) easterly subsurface inflow from Garland Flat (Van Denburgh et al., 1970). The waters that are present at this spring interact with the Luning Formation, composed primarily of limestones and shales (Ross, 1961). This spring is several hundred meters to the east of the regionally significant Benton Springs Fault that accommodates up to half of the total regional deformation (Angster et al., 2019; Koehler et al., 2021). Multiple surface ruptures caused by normal and right-oblique slips were recorded during May 2020 by Koehler et al. (2021). The Mina site experienced seismic intensities of V-VI during the initial shock (Figure 2) (*U. S. Geological Survey Earthquakes*, 2020).

v. Other Sites

Two other sites were visited in response to the May 15th, 2020 earthquake. These sites are an ephemeral seep located in Garfield Flats (Garfield Spring), west of state highway 95 and north of the Candelaria hills, and an artesian spring near Soda Springs, Nevada (referred to as the Tony Tipton Property) (Figure 2A). The Garfield Spring is located 40 km NW from the epicenter, while the Tony Tipton Property is located 28.75 km NNW from the epicenter (Table 2). Both of these sites were in the intermediate field of the May 15th earthquake (Figure 2A). Additional sites were visited during the first 2 weeks after May 15th, 2020, including some low flow springs and seeps, but these were deemed unsuitable for the study because there was no point source to sample the water directly before it flowed into a meadow or pool. The sampling conducted during the study began during the height of the COVID-19 pandemic shutdown, and this limited access to potential municipal sources.

2. Materials and Methods

A. Field Sampling and Sample Preparation

Monitoring was conducted beginning on May 16th, 2020 through December 2021, and was initially conducted at weekly intervals, decreasing to every two weeks in late summer 2020. Monitoring frequency was again increased immediately following the seismic activity in November and early December 2020 before decreasing to monthly intervals for the entirety of 2021.

During the initial reconnaissance trip on May 16th, 2020, temperature, flowrate, pH, and specific conductance (SpC) were measured and water samples were collected for elemental water chemistry from two of the sites the Fish Lake Valley hot well and the

Mina Dump site. During the next sampling trip (5/22/2020) monitoring began at the Columbus Marsh site and pH measurements were added as part of the monitoring routine at all sites. Five weeks after the initial event (6/20/2020), the Willow Ranch site was added to the monitoring regime. Finally, alkalinity was added to the monitoring routine for all sites beginning on June 27th, 2020.

Physiochemical parameters were recorded at each site during each monitoring effort and values are provided in Appendices 1 through 7. Temperature, SpC, and pH were measured using a YSI 556 Multiprobe System (YSI). The YSI was calibrated the morning of sampling using a one-point calibration for SpC (1 mS/cm) and a two-point calibration for pH (pH 4 and pH 10). An additional measurement of temperature was taken at each site using a mercury thermometer to provide a crosscheck of the temperature reading from the YSI. All temperature measurements were found to be in agreement. Alkalinity was measured using a colorimetric titration method with a Hach Alkalinity Kit. When sampling a spring, flowrate was recorded by timing how fast flow filled up a 10 L bucket. The bucket was filled a total of three times, and the average time was used in the analysis.

A total of five water samples per site were taken on each sampling trip for isotopic and elemental chemistry. One 125 ml bottle was taken for anion concentrations, a second for cations (acidified with 2 ml of 1:1 dilution HCl), and a third 125 ml bottle was sampled for $\delta^{13}C$ analysis of dissolved inorganic carbon ($\delta^{13}C_{DIC}$ or DIC). A 20 ml dram was filled for deuterium and oxygen ($\delta^{2}H$ and $\delta^{18}O$) isotopic analysis. Lastly, a 1 L sample was taken and used for alkalinity testing (100 ml) and as a backup in case any of the other samples needed to be retested or were lost. All samples except for the 1L sample were filtered on site using a 0.45 µm nylon (NY) opening syringe filter. Alkalinity testing was conducted using a Hach Alkalinity Kit using a titration method. The ion

samples were sent to the University of Insubria in Como Italy, where our collaborators Pozzi, Binda, and Trotta ran analyses and interpreted these data. The groundwater isotope samples were submitted to the stable isotope lab at the University of Reno, Nevada.

In the lab, water samples collected for $\delta^{13}C_{DIC}$ analysis were basified by introducing and dissolving ACS grade sodium hydroxide pellets. This treatment produced carbonate from any bicarbonate dissolved in the water. Samples were then mixed with strontium chloride which reacted with the carbonate to produce solid strontium carbonate which precipitated. The samples with the precipitated strontium carbonate were poured into a vacuum filtration system and then filtered through a 0.45 µm MCE filter. Strontium carbonate residue left on the filter was scraped off and put into drams. The strontium carbonate samples were dried in an oven overnight at 50 °C. Strontium Carbonate samples were then given to the UNR stable isotope lab for $\delta^{13}C_{DIC}$ isotopic analysis.

B. Climatological Data Analysis

In order to fully interpret physiochemical changes throughout the timeseries, a climatological data analysis was conducted for each basin to identify potential changes in groundwater that may be related to. The Standardized Precipitation Index (SPI) and Standardized Precipitation-Evapotranspiration Index (SPEI) were calculated and correlated to well water measurements made within several hydrographic basins surrounding the area of interest (Abatzoglou, 2011; McKee et al., 1993; Sienz et al., 2012; Stagge et al., 2015; U. S. Geological Survey, 1994).

SPI is calculated using a method of comparing probability to climatic precipitation observations. For this study, the range for precipitation data is from January 1st, 1980

through January 15th, 2022 (~42 years). An accumulation period of precipitation is then selected which represents the amount of time it takes for precipitation to influence well water changes. Factors such as well location and basin recharge were taken into account to determine what timeseries of climate index best fit well water variations in each setting. I selected four periods to compare: a 180-day, 1-year, 2-year, and 5-year period for each hydrographic basin. Upon selecting an accumulation period, the summation of previous rainfall is applied to each precipitation event. These values are fitted to a Gamma function/a parametric distribution, and a probability is assigned to each event. The result is a series that measures deviation from "normal conditions" expressed in standard deviations (Abatzoglou, 2011; McKee et al., 1993; Sienz et al., 2012; Stagge et al., 2015). One standard deviation from normal is considered "moderate", whereas two standard deviations is considered to be "severe" conditions.

The same methods used in the calculation of SPI are applied to measure the probability of SPEI. However, instead of only summing the precipitation values for each accumulation period, the net water input is calculated as the difference between precipitation and Potential Evapotranspiration (PET). For this study, the PET was calculated using the methods described in Thornthwaite, (1948). This method uses very few climate variables: temperature, heat index, and the angle of the sun (Abatzoglou, 2011; Vicente-Serrano et al., 2010). The Thornthwaite method is useful for locations of limited data, meaning it can be applied nearly anywhere. That being said, one downside to using this method is that it is not as accurate as other methods. Given the remote nature of this study this appears to be the best available method.

Instead of calculating climate indices for each site, climate indices were provided by the publicly accessible GridMET dataset. This dataset is based on the calculation of climate variables using a large array of climate stations. The calculations are made on a

4 km grid space. Each hydrographic basin was incorporated into the model, which gave back the mean climate variable (SPI and SPEI) across the specified region (Abatzoglou, 2011; Huntington et al., 2017).

The wells in the surrounding hydrographic basins are used as proxies to best-fit the climate index to long-term groundwater measurement data. Historical well water measurements were obtained from National Water Information System data. To correlate the climate and water level datasets, methods were utilized from (Leelaruban et al., 2017; U. S. Geological Survey, 1994). Here, the two datasets are correlated using a Pearson correlation as both datasets are, for purposes of this study, considered "interval" data. As water level measurements that were used in this dataset were taken in feet below ground, an ideal correlation for the data should be -1. This means that with a decrease in climate index value (indicating a drought) a greater groundwater reading is expected. This study found that in this region the 2-year and 5-year accumulation period best fit the groundwater level data. Therefore, both 2-year and 5-year SPEI were evaluated for each site for the duration of the sample period.

C. Static Strain Analysis

i. May 15th Event Model

Geodetic models were created both around the main M 6.5 event, and for several aftershock periods which were host to earthquakes >M_w 5 that followed in 2020. Modeling of the main event was conducted by Crandall-Bear & Hammond, (2021). Their model was developed using both Global Positioning Systems (GPS) and Interferometric Synthetic Aperture Radar (InSAR) data used to accurately measure ground displacement. The GPS data was provided by the semi-continuous MAGNET GPS Network (Blewitt et al., 2009). In addition to regional conintuous GPS networks, primarily

the NSF EarthScope Network of the Americas, the nearest station of which P627 is ~40 km from the M 6.5 epicenter (UNAVCO Community, 2007). InSAR data was provided by the European Space Agency. By quantifying surface displacements at GPS stations with mm accuracy using both the GPS and in blanket coverage of the landscape using InSAR with cm accuracy, they solved for the fault parameters in an elastic half-space dislocation slip model Okada (1985). Here, the seismic moment, the location of the epicenter, depth, strike, and dip of the slip are inferred. This model is used to predict on a regular grid of nodes with 1 km spacing the horizontal surface displacement that resulted from fault slip. From the predicted displacements, I calculated co-seismic using displacements within a 5.5 km radius of each sample site.

ii. Aftershock Sequence Models

Similar to the main shock, I modeled surface displacements on an array of nodes following seismic clusters occurring later in 2020. Due to the much lesser magnitude of the later seismic events, GPS data was not able to accurately measure surface displacements, and therefore it was not possible to infer the slip parameters from geodetic data. The following calculations were applied to estimate the fault parameters (Hanks & Kanamori, 1979[1]; Wells & Coppersmith, 1994[2][3][4]):

The first equation estimates the moment magnitude of the event given the seismic moment provided by the U.S. Geological Survey and the Nevada Seismological Laboratory (*Events*, 2010; *U. S. Geological Survey Earthquakes*, 2020).

[1] $M_O = 10^{\frac{3}{2}*(M_w+10.7)}$

Where:

M_w is the moment magnitude

M_O is the seismic moment [dyne-cm, then converted to N-m]

A second equation models fault plane parameters.

[2] $L = 10^{(\frac{M_W - 5.08}{1.16})}$

Where:

L is the length of the fault plane [km]

M_w is the moment magnitude

For this model it is assumed that the width and length of the fault plane are equal.

A third equation was then implemented to estimate displacement along the fault plane.

[3] $D = \frac{M_O}{A * \mu}$

Where:

D is the average slip across the fault surface [m]

A is the area of the fault plane [km^2]

μ is the shear modulus of the crust of the earth [Pa]

Finally, a fourth equation is used to find the depth of the top of the fault plane given the depth of the epicenter of the event provided by the U.S. Geological Survey and the Nevada Seismological Laboratory (*Events*, 2010; *U. S. Geological Survey Earthquakes*, 2020).

[4] $dTop = d_{ep} - \frac{W}{2}$

Where:

$dTop$ is the depth from the surface to the top of the fault plane [km]

d_{ep} is the depth of the epicenter of the earthquake [km]

W is the width of the fault plane [km]

Using the above earthquake parameters, interpreted from moment tensor data provided by the U.S. Geological Survey and the Nevada Seismological Laboratory, I estimated the amount of slip the fault experienced was calculated and used as the basis for a slip model on a dislocation in an assumed elastic half space, similar to the one used for the May 15th, 2020 event (*Events*, 2010; *U. S. Geological Survey Earthquakes*, 2020; Okada, 1985).

A total of three aftershock sequences were found to be significant as these sequences induced a hydrologic response toking place in June, November, and December 2020. All three were part of seismic clusters with one or more shocks > M_w 5. Moment tensors were provided by the Nevada Seismological Laboratory, and the U. S. Geological Survey (*Events*, 2010; *U. S. Geological Survey Earthquakes*, 2020). For earthquakes without available moment tensors, moment tensor parameters from immediately surrounding, representative events were used.

Just as applied to the main shock, the surface displacement of these events predicted from the moment tensors were used to calculate the strain at each sampling location. Strain was calculated at each site for each aftershock sequence by analyzing surface displacements within a 5.5 km radius surrounding each sample location. The surface displacements from each individual earthquake > M_w 4 within each sequence were summed by aftershock sequence (June, November, and December). The result of which represented the total co-seismic surface displacement as a result of several > M_w 4 events over the course of two days surrounding the largest shock.

3. Results

A. Physiochemical Measurements

The major changes in physiochemical parameters and water isotopes are plotted as time series graphs on Figures 12 and 13. The full suite of results for all parameters measured and analyzed are tabulated in Appendices 1 through 7. A synopsis of the main responses is discussed below.

i. Specific Conductance

Specific conductance values vary widely between sites, from the high conductivity Columbus Marsh site where values reached as high as 4.8 mS/cm, to the low conductivity Willow Ranch site, where values were just under 0.2 mS /cm (Figure 12B) (Appendix 1). The SpC measurements show apparent responses in association with all four of the >M_w 5 events, although there are differences both spatially and temporally. The most pronounced responses were seen at the high conductivity well at the Columbus Marsh site with the implied decreases in SpC in association with the May 15th, and observed decrease associated with the June 30th and November 30th events. In contrast, SpC rose sharply at Columbus Marsh following the December 2nd event. The Columbus well is periodically pumped to fill water trucks and also provides water for the nearby Ireland Minerals plant. Water withdrawal dates and usage are metered and logged at the site and are plotted on Figure 12 (dashed lines). The Columbus Marsh data show no effect on changes in SpC.

Personal communication with Tom Miller, Ireland Minerals plant manager, indicates that a nearby well that is drilled deeper in the valley floor produces much brinier (high conductivity) waters than those recorded at the Columbus Marsh site, but was not sampled.

Fish Lake Valley is farther away from all of the events relative to the Columbus Marsh site, and showed subtler changes in SpC. The most notable response of which was to the November and December events.

The SpC at the Mina and Willow Ranch sites were the least affected, showing little changes, across the June, November and December events. The Willow Ranch monitoring did not begin until five weeks after the May 15th event, and consequently any effects in association with the main shock are unknown.

ii. Alkalinity

Alkalinity, like SpC, also records some changes in response to the events (Figure 12C) (Appendix 2). Alkalinity data were not collected until after the main M 6.5 shock, and can only be evaluated for the June 30th, November 13th, and December 2nd events. Alkalinity values ranged from as high as 280 mg/L $CaCO_3$ at the Columbus Marsh site, to 64 mg/L $CaCO_3$ at the Willow Ranch site. Overall, some responses in alkalinity are noted, however, there is more variation in alkalinity in between seismic events (Figure 12C) than what was observed for the SpC data (Figure 12B).

iii. Temperature

Temperature measurements showed some variation across the monitoring period at all sites (Figure 12D) (Appendix 3). The thermal well at the Fish Lake Valley site recorded a ~3.5 °C variation, from 36-39.5 °C. The other sites were more stable, with a few short-lived temperature spikes. One notable spike occurred at two sites, Columbus Marsh and Willow Ranch on October 30th, two weeks prior to the November 13th event. Temperature then dropped rapidly by the November 14th sampling. At Willow Ranch, this spike was the most pronounced, rising 3.8 °C from October 11th to October 30, 2021, then dropping ~5 °C on November 14th.

iv. pH

pH values varied across the entire time series and indicated a strong correlation between all sites (Figure 12E) (Appendix 4). The Fish Lake Valley hot well, the thermal well, had consistently higher values than the other sites. The variation appears to have a seasonal pattern, with the lowest pH values observed in the fall of both 2020 and 2021. The most significant variation was observed at the Columbus site in association with the November and December events. However, there were equally large changes between events, making it difficult to evaluate pH data in relation to seismicity.

v. Flow Rates

Two of the sites, Mina Dump and Fish Lake Valley had artesian flow that could be readily measured. Flow rates varied for the Mina site with a high of ~8 E-4 m^3/s in the early summer of 2021 and low (5.7 E-5 m^3/s) values in the Fall of both 2020 and 2021. In 2021, flow had ceased entirely by October (Figure 12F) (Appendix 5). The flow rates at Fish Lake Valley also varied, although more modestly, from 1.85 E-4 to 2.15 E-4 m^3/s. The changes at Fish Lake Valley appear to correlate in part to seismicity, with a small drop observed after the seismic event in November 2021 (Figure 12F). The seep at Garfield Spring was first observed on 5/26/2020 and had completely dried up on 7/9/2020. At the Tony Tipton Property, increased artesian flow was observed following the May 15th event and persisted for several months.

B. Isotope Data

Oxygen and Hydrogen isotope data for each of the sites are presented in time series (Figure 13) and error bars represent the uncertainties in values on Figure 13A. Uncertainties don't exceed 1 ‰ for δ^2H and 0.5 ‰ for $\delta^{18}O$. The most notable changes, short-lived negative excursions in both δ^2H and $\delta^{18}O$ (around -0.9 and -0.3 respectively),

were inferred to take place in association with the May 15th and observed in association with the June 30th events at the Columbus Marsh (Figures 12 & 14) (Appendix 6).

Variations seen in $\delta^{2}H$ values are within the uncertainty of the analysis, but they track with the changes in $\delta^{18}O$ so the signals are deemed to be valid.

Additionally, $\delta^{2}H$ and $\delta^{18}O$ are plotted relative to both the Local Meteoric Water Line (LMWL) and Global Meteoric Water Line (GMWL) (Craig, 1963; Lachniet, 2020). Evaporation lines are shown to infer intersection with the LMWL (Figure 14).

$\delta^{13}C_{DIC}$ isotope data from this analysis did not show any discernable response to seismicity through the first year of data collection. Sample values at the Willow Road well and the Columbus Marsh well did show some changes through November and December, although drivers for this response are unknown (Appendix 6).

C. Climatological Analysis

Throughout the dataset, Hydrographic Basins 118 and 121A showed a steady drying trend as SPEI values became more negative (Table 5). The 2-year and 5-year SPEI data through early to mid-2020 suggest somewhat “normal” climate conditions (Figures 2 & 15). Both basins began to experience moderate hydrologic deficits from October 2020 through the end of the year. Severe drought conditions began in both basins in June 2021.

Hydrographic Basin 117 showed “normal” climate conditions throughout the entirety of the year based on both 2-year and 5-year SPEI data (Table 5). By February 2021, the 2-year SPEI within this basin dropped to moderate drought conditions (Figures 2 & 15). In June 2021, severe drought set in. These drought conditions remained steady throughout the remainder of the data period. When analyzed for the 5-year SPEI, Hydrographic Basin 117 suggests only moderate drought conditions in June 2021. By

July 2021 wetter conditions began to set in, and by December 2021, conditions returned close to “normal”.

D. Static Strain Analysis

Results of the strain analysis are summarized in Table 3 and presented for the May 15th (Figure 16), June 30th (Figure 17), November 13th (Figure 18), and December 2nd (Figure 19) events, the aftershock sequences that hosted earthquakes > M_w 5. Uncertainties in the measurements of coseismic displacement for the May 15th event are between +/-0.33 and +/-1.72 mm, which are within the measurement of modeled displacements throughout the study area. Co-seismic displacements for the aftershock sequences are solely based on model predictions, and therefore do not have uncertainties related to them.

i. May 15th, 2020

During the May 15th event, the special distribution of earthquakes was spread nearly evenly across the eastern extension of the Candelaria fault (Figure 16). The M 6.5 shock occurred on the more eastern portion of the fault (Figure 2), at a depth of only 2.7 km (Table 4). One event > M_w 5 followed, and was located just north of the main shock. The magnitude of static strain, as well as the distribution of modeled surface displacements as a result of the main shock are shown on Figure 16. Both horizontal and vertical displacement was the greatest immediately surrounding the Columbus site (Figure 16B & 16C). The greatest positive vertical displacement was seen on the north side of the Candelaria fault, while the greatest negative vertical displacement was seen on the south side (Figure 16C).

The Columbus site experienced the largest amount of strain (1.20 E4 nanostrains) from the May 15th, 2020 earthquake, where strain values were two orders

of magnitude greater than the other principal sample locations. All sample sites except the Mina Dump Road site experienced positive horizontal dilatation. The magnitude of the contraction observed at the Mina Dump Road site (339 nanostrains) was nearly equal to the magnitude of dilation observed at the Willow Ranch and Fish Lake Valley sites (511 nanostrains for both) on May 15th (Figure 16A).

The two sites where groundwater discharge was also observed (the Garfield Spring and the Tony Tipton Property) were modeled for this event. These sites experienced contraction of 673 and 1.21 E3 nanostrains, respectively (Figure 16A) (Table 3).

ii. June 30th, 2020

Renewed seismicity on June 30th, 2020 was minor, with only one shock equaling M_w 5 around 8.3 km deep (Table 4). The seismic events that took place during this time were predominantly on the eastern side of state Highway 95, with the epicenter of the largest event located nearly under the highway (Figures 2 & 17). The magnitude of static strain, as well as the distribution of modeled surface displacements as a result of the June 30th seismicity are shown on Figure 17A through 17C. The distribution of both the horizontal and vertical displacements were centered on Highway 95, with the larger displacements taking place on the western side of the Highway (Figure 17B & 17C).

Similar to the May event, model suggests for the June 30th, 2020 event indicated strain at Columbus that was two orders of magnitude greater than the other sites. The model suggests that both Mina Dump site (4.10 nanostrains) and Columbus Marsh (220 nanostrains) underwent net contraction.

Willow Ranch (5.84 nanostrains) underwent slightly more strain than the Fish Lake Valley site (4.74 nanostrains), but both located within the region where the model suggests positive net dilatation, and are within the same order of magnitude (Figure

17A) (Table 3).

The Garfield Spring and the Tony Tipton Property were also modeled for the June 30th event. These sites experienced contraction of 8.07 and 11.3 nanostrains, respectively (Figure 17A) (Table 3).

iii. November 13th, 2020

The November seismicity was farther east than the other events, occurring exclusively on or eastward of the M 6.5 shock. Several > M_w 4 and a M_w 5 event took place (Figure 18) at depths between 4 and 10 km during this sequence (Table 4). The magnitude of static strain, as well as the distribution of modeled surface displacements as a result of the November 13th seismicity are shown on Figure 18A through 18C. Since the epicenters were predominantly located to the east, the surface displacement model suggests that the majority of the deformation was also east of all sample sites (Figures 2, 18B, & 18C).

During the November 13th event, the Columbus Marsh experienced 122 nanostrains of positive net dilatation, equal but opposite of the amount of strain experienced during the June 30th, 2020 events. Positive net dilatation was also observed at the Willow Ranch (15.4 nanostrains) and Fish Lake Valley sites (20.6 nanostrains). The Mina Dump site (22.8 nanostrains) is the only site that experienced contraction during this event (Figure 18) (Table 3).

iv. December 2nd, 2020

On December 2nd, 2020 a series of > M_w 4 and > M_w 5 shocks occurred (Figure 19) between 4-5 km depth (Table 4), 20km west of the initial M 6.5 shocks of May 15th and November 13th events. The magnitude of static strain, as well as the distribution of modeled surface displacements as a result of the December 2nd seismicity are shown on Figure 19A through 19C. The distribution of both the horizontal and vertical

displacements were centered near the ghost town of Candelaria (Figures 2, 19B, & 19C), with the larger displacements taking place on the western side of Candelaria. Due to the location and orientation of seismicity, the amount of strain most sites underwent was less than that experienced during the June 30th, 2020 aftershocks, despite the relatively greater magnitude of several of the December 2nd shocks.

In December, the Mina Dump Road spring, Willow Ranch, and Fish Lake Valley sites all experienced positive net dilatation with the Columbus site experiencing net contraction. This fourth event generated the least amount of strain observed for the four monitoring sites. Columbus had the largest strain with only 44.6 nanostrains of contraction occurring around the site. Fish Lake Valley experienced the least amount of strain with 0.63 nanostrains of dilatation. Willow Ranch and the Mina Dump Road sites experienced 8.45 nanostrains and 3.17 nanostrains of positive dilatation, respectively (Figure 19A) (Table 3).

4. Discussion

A. Non-seismic Variation

In order to determine the seismically-induced mechanisms of physiochemical changes recorded in this study, these effects must first be separated from those related to climate and seasonality, and discuss groundwater properties specific to each basin.

i. Seasonality and Climatic Controls

Recharge processes within the Great Basin are largely driven by winter precipitation which is stored in the form of snowpack until the spring/early summer months. Processes that recharge each basin are complex and vary between sites in basin 117. They depend largely on the geology of the surrounding mountains and local

fault parameters. The two primary recharge forms also depend on climatological factors controlling local melt rates. Basins may receive recharge percolating into the ground from the mountains, or they may receive recharge during great melting events in the form of intermittently flowing alluvial streams (Harrill & Prudic, 1998).

During this study, SPEI values showed that all of the sample sites were experiencing conditions that were drier than normal, particularly during the second year (Figure 15) (Table 5). Locations with less recharge tend to have a slower groundwater flow along prevailing flow paths (Fetter, 2018). This can be attributed to the lower driving hydraulic heads over any given distance (Fetter, 2018). Slower flow rates allow for a greater amount of time for groundwater to interact with bedrock, leading to water samples having higher concentrations of total dissolved solids (TDS) and therefore higher SpC. The longer watershed interaction time can also result in more evaporative signatures in $\delta^{2}H$ and $\delta^{18}O$ isotopes. Slower groundwater flow rates may also cause transient effects of seismicity to be delayed as it would take longer for evidence of those effects to be transported from its source area to the sampling location. However, evidence of increased groundwater interaction with bedrock, increased evaporative signatures in $\delta^{2}H$ and $\delta^{18}O$ isotopes and delays in geochemical signals were not seen throughout this study.

During wetter periods, when hydraulic heads are greater, flow rates are faster and flow volumes increased, the transient signals may not be detectable as the signal may be flushed from the groundwater system before the next sampling effort. Higher positive SPEI values, particularly during the winter months (October through March) would result in greater recharge for that year (Table 5). Signals may be diluted by the greater amounts of water, a factor that could have played a role in the lesser reaction in groundwater observed at the Mina Dump Road site to the June 30th seismicity (Figures

12 & 15).

Seasonally-driven changes in flow rates were observed at the Mina Dump Road site (Figure 12F) with the lowest flow rates observed at the end of the water year. Within the Basin and Range, a water year is defined as being the cutoff between the end of the dry season (April to September) and the beginning of the wet season (October to March). After experiencing moderate to severe drought conditions throughout early to mid-2021, groundwater flow at the Mina Dump site had stopped by October 2021.

Temperature readings from Mina show a modest response to seasonality with cooler temperatures recorded in the winter months which may be consistent with rapid recharge and flow (Figure 12D). In contrast to Mina, the site with artesian flow, the Fish Lake Valley hot well, showed no seasonal change in discharge, and only a slight drop in winter temperatures (Figures 12D & 12F). The difference in the apparent seasonal effects on flow rates likely relates to the flow paths. Mina recharge is largely from surficial runoff, while the Fish Lake Valley hot well taps a relatively isolated confined thermal aquifer with longer and deeper flow paths. This may buffer the seasonal variation in recharge from its distal recharge area which is located at the base of the White Mountains (Figure 8B).

ii. Basin-specific Characteristics Affecting Groundwater Properties

The principal sites span three hydrographic basins. Sampling has revealed geochemical signatures that suggest similarities and differences in recharge and flow paths in these basins (Figures 2 & 8). These attributes will need to be considered when trying to interpret groundwater response to seismicity.

a. Fish Lake Valley Hydrographic Basin

The Willow Ranch site and Fish Lake Valley hot well are both located within the Fish Lake Valley Hydrographic Basin. However, aquifer types and recharge processes

vary between these two sites.

Recharge at the Willow Ranch site is largely from intermittent flowing streams originating from the eastern face of the White Mountain Range and also from precipitation that falls directly on the valley floor. Water flowing from the Fish Lake Valley hot well also originates from the eastern face of the White Mountains, but instead it probably seeps into several permeable North-South oriented faults present at the base of the mountain range. Here, the recharge enters a deeper aquifer where flow paths bring them towards the center of the valley floor. The Fish Lake Valley hot well is located farther from the base of the mountain range (~15 km from the White Mountains) than the Willow Ranch site (~10 km from the white mountains) and is structurally below the Willow Ranch water withdrawal depth (Harrill & Prudic, 1998) (Figure 4B).

$\delta^{2}H$ and $\delta^{18}O$ isotope signatures for the Willow site likely result from large precipitation or recharge events as they represent values closest to that of the LMWL of the four study sites (Figure 14). Large amounts of runoff are required to cause flow in the intermittent streams that recharge the valley aquifer (Van Denburg and Glancy, 1973). In contrast, the Fish Lake Valley hot well has values that have a more signal, suggesting longer atmospheric exposure prior to infiltration (Craig, 1963). Intersection of the Willow site water samples with the LMWL also suggests a lower recharge elevation than that of the Fish Lake Valley hot well, which would be consistent with the proposed differences in recharge areas discussed above.

b. Columbus Salt Marsh

Groundwater from the Columbus Salt Marsh site, which is located within a terminal hydrographic basin, has the highest SpC values, but no clear seasonal effects were recognized. Flow paths indicate a hydrologic connection to waters from the Fish Lake Valley to the south. As such, both sites have water isotope values that plot closely

together and both sites show water isotope signatures typical of extensive evaporation (Figures 8A & 8B & 14).

Groundwater pumping does not appear to influence the physiochemical response recorded at the Columbus Marsh site. Well water withdrawal was tracked beginning in July 2020. The nearby mining facility utilizes this well for operations, and additional water was withdrawn for road work in June 2020. Comparing the pumping schedule to the tested parameters, it doesn't appear that there is any correlation with well water withdrawal and thus, drawdown (Figure 13).

c. Eastern Soda Spring Basin

The Mina Dump Road spring, like the Columbus and Fish Lake Valley sites, shows a more evaporative signal (Figure 14). Projection of values to the LMWL suggests a recharge elevation lower than the other sites. Flow is highly controlled by seasonality as this spring has a small recharge area and is sourced locally from shallow waters.

B. Differential Responses Related to Attenuation

Seismic intensity changes with distance from the epicenter based on the attenuation-distance relationship (Manga & Wang, 2015; Lay & Wallace, 1995). The epicenters of all four seismic events with >M_w 5 earthquakes are located along on an east-west series of faults within the Columbus Marsh hydrographic basin. The faults are located closest to the Columbus well, and more distant from the other sites. This variability provides an opportunity to qualitatively gauge attenuation effects on hydrographic responses observed between monitoring sites.

Table 2 shows the distance between each site and the epicenters of all four events. The Columbus Marsh well was in the near field, between 5 and 15 km from each of the epicenters. This site showed some of the greatest physiochemical response to

seismicity, as would be expected. Given that the seismic intensity in the basin was ~VIII, for the main shock, the highest intensity reported for the four events (Figure 2). In contrast, the Mina and Fish Lake Valley hot well sites were more distal, situated between 30-38 km from the epicenters, and were located in separate hydrographic basins. The Willow Ranch was slightly farther away, ~40 km from the epicenters. Distance alone may account for the considerably weaker responses at the Mina, Willow, and Fish Lake sites, but other factors such as focal depth, bedrock depth, site elevation, groundwater depth and flow paths, and the nature of porous medium may also play a role in this relationship.

Not all events caused observable changes in groundwater. The potential effects of the M 6.5 shock cannot be fully gauged at the more distal sites because of the lack of data for the time period immediately preceding the event. However, there are small discernible effects noted for the November and December events, indicating that a M_w 5 event can register a change in temperature and SpC within a 40km radius. This has useful implications for designing future seismic hydrochemical monitoring systems.

C. Role of Strain in Differential Hydrochemical Response

i. Changes Related to Dynamic Strain

Mechanistically, since dynamic strain is related to intensity of seismicity, the best time to identify changes related to this process is to analyze data in the early part of the seismic series, when intensity is highest. As mentioned before, and shown in Figure 3, May through early June, 2020 is the period with the greatest release of seismic moment, or energy. (*U. S. Geological Survey Earthquakes*, 2020).

The Columbus Salt Marsh site, which was in the near field of these events, indicated an observed depletion of groundwater isotope and SpC values on May 22nd

and June 27th, 2020. This observation could potentially represent a change in source water during a time when there was an intense period of shaking (Figures 3 & 13A).

In their established field area, Koehler et al. (2021) mapped fractures and ground ruptures that were predominantly east-west trending, following the orientation of the responsible faults as well as the Candelaria Hills. Although not observed during this event, fractures may be present between the base of the Candelaria Hills and the Columbus Marsh well. If water-bearing fractures and faults in this hydraulically upgradient area were affected and made more permeable, they may be holding back potential recharge water derived from the Candelaria Hills. The waters held in the Candelaria Hills would have had lower concentrations of SpC as they had yet to interact with the basin, and these waters would also be expected to have a less evaporative groundwater isotope signature. This mechanism provides a possible explanation for the drop in SpC accompanied by the depleted water isotope values in May 22nd and June 27th, 2020.

Signals of depleted isotope concentrations were not observed in the later portion of the seismic event series may be partly explained by a couple of factors. First, the greatest seismic intensity of shaking occurred earlier in the sequence and there may be a threshold level below which there is no response (Figure 3). This can be related back to the driving mechanism for the observed changes. Second, if fracture unclogging was the mechanism responsible for increased flow, then a decay in hydrochemical signal would be expected with time. This may be because there may not be any more significant fractures left to unclog, or because of insufficient time for unclogged fractures to develop substantial sedimentation of colloidal material. Continued shaking throughout 2020 may have mitigated deposition of material in these fractures.

In addition to fracture unclogging in the Columbus Marsh, dynamic strain had

driven liquefaction to occur (Manga & Wang, 2015). Following the initial event, liquefaction was modeled to be most probable in the Columbus Marsh area following the first event (*U. S. Geological Survey Earthquakes*, 2020).

Another significant observation early in the seismic series that may be related to dynamic strain pertains to flow rates at the Mina Dump spring in May through June 2020 (Table 3) (Figure 12F). The Mina Dump site shows a strong meteorologically-driven pattern in flow rate, with peak flow occurring in the spring to early summer, following spring runoff. However, differences in both the timing and magnitude of peak flow between 2020 and 2021 may be attributed to the introduction of seismic stresses. The magnitude of peak flow in 2020 is less than in 2021 (Figure 12F), despite the fact that 2021 had the more severe drought conditions as shown by the SPEI analysis (Figure 15C). If peak flow were completely driven by meteorological patterns, then the magnitude in 2020 should have been greater, not lesser than 2021. Moreover, the peak flow occurred earlier in in 2021, during May and June. In contrast May and June of 2020 experienced high seismic activity, which may have had a dampening effect on flow rates, delaying the peak flow until July (Figure 12F).

Given the weak response to transient changes in physiochemical effects at the Mina Dump site throughout the remainder of the timeseries, the flow effects may be best attributed to dynamic strain. Here, dynamic strain led to the dampened flow rates through the consolidation of the low pore pressure, shallow groundwater system or through the agitation of loose sediments which led to the blocking of flow paths. This process is particularly expected in alluvial deposits where this artesian spring is located (Brodsky, 2003; Manga & Wang, 2015). Dynamic strain was most intense during this part of the seismic sequence as shown in Figure 3. During the first several months of seismicity following the main event, the slope of the cumulative moment magnitude

released during the sequence was the steepest.

As described below, static stress changes at Mina may have also played a role. The modeled static strain at Mina was contractional for all events with the highest magnitude experienced during the May 15th event (Table 3). The comparatively high contractional strain in May could have had a transient effect in reducing flow from May to July 2020.

ii. Changes Related to Static Strain

Perhaps the best example observed of the contrasting effects of strain is the differential response observed at some of the sites between the November and December 2020 events. On November 13th there was a decrease in SpC and pH at the Columbus Marsh site with a lack of any changes related to groundwater isotopes (Figures 12B, 12E, & 13). This site experienced dilatation during this time (Table 3). In contrast, co-seismic strain was contractional during the December 2nd event. As a result, the trend in these geochemical parameters at the site reversed and returned back to readings seen prior to the November 13th event (Figure 12B & 12E). This differential response at the Columbus Marsh frames the importance of the sign of strain a site is experiencing.

The Fish Lake Valley hot well also experienced dilatation on November 13th. Similar to the Columbus Marsh site, a decrease in SpC was observed over the two weeks following the event (Figure 12B). Despite an apparent lack of contractional strain at the Fish Lake Valley site on December 2nd, there was also a reversal in the SpC trend (Figure 12B).

From the strain analysis of the Willow Ranch site on December 2nd, it is known that dilatational strain was taking place nearby Fish Lake Valley hot well (Table 3). The proximity of this dilatational strain in relation to the Fish Lake Valley hot well may have

played a role in reversing the effects of mixing at the site by restabilizing pore pressure around the well location as the pressure gradient migrated towards the dilatational environment (Figure 20). The fast response to the December 2nd event may be due to increased permeability resulting from the dilatational November 13th event.

Both the November and December events were composed of a number of smaller events. The December events were slightly more numerous and protracted, but comparable in the magnitude of strain in November (Table 3). One major distinction between these two events was in the sign of the static strain at the Columbus Marsh site. Another distinction was the relative location of the epicenters which were located in different areas along the fault, which may have shifted the geometry of the strain field and direction of fluid flow at the Fish Lake Valley hot well (Figures 2B, 17, & 19).

Changes in physiochemical parameters such as those discussed above suggest groundwater mixing (Figures 12B & 12D). Without changing water isotope concentrations, it can be concluded that this mixing is taking place within the aquifer (Figure 13A). As stated above, dilatational static strain can cause changes in pore pressure causing downwelling along the pressure gradient. On the other hand, contractional strain can upward movement of fluid (Manga & Wang, 2015). The observations support the inferred mechanism for observed SpC changes in a chemically stratified aquifer resulting from groundwater mixing within the aquifer.

Another response to co-seismic contractional strain in the area north of the Candelaria Hills occurred following the May 15th event. Increased groundwater flow rate occurred at two locations, the Tony Tipton Property and the Garfield Spring. Model analysis indicate that both of these sites experienced contractional strain, with the highest strain modeled at the Garfield Spring (Table 3). The observed increases in flow rates are consistent with what would be expected in a contractional environment.

iii. Precursory Signals

Contractional stress even in the absence of measurable strain may have a direct impact on pore pressure. The introduction of stress influences fluid flow to balance forces applied on the system. Similar to the effects of strain, stress may induce upward movement of fluid. Increases in groundwater temperature have been connected to changes in stress within aquifer systems, owing to the upward migration of thermal waters (Archer et al., 2019; Binda et al., 2020; Manga & Wang, 2015). This mechanism may possibly explain the transient increase in temperature at both the Columbus Marsh site and the Willow Ranch site on October 30th, 2020 (Figure 12D). The change in static stress on November 13th, measured by dilatational strain at both sites (Table 3), may have relieved the buildup of pore pressure, thus this transient anomaly may be considered precursory, given that it preceded the November 13th event by two weeks. The temperature anomaly was short-lived and temperature returned to baseline values by November 14th.

The temperature increase at the Willow Ranch site may be explained by the upwelling of geothermal waters from below, from which the Fish Lake Valley hot well is sourced. However, this explanation is not entirely satisfactory, because there does not appear to be geochemical evidence of mixing nor introduction of Fish Lake Valley thermal waters into this well in association with the October 30th temperature anomaly. The cause for the increase in temperature at the Columbus Marsh is thus speculative due to a lack of data from below the well source. While the effects of aseismic stress buildup may be a plausible explanation, more investigation is needed to further test this hypothesis.

iv. Mechanisms Observed by Others

In addition to the effects of strain, there are co-seismic crustal processes that

may be triggered by earthquakes, which in turn may impact the groundwater hydrochemistry. These are reviewed briefly in Binda et al. (2020) in terms of modern hydrochemical responses and in Archer et al. (2019) in relation to paleolimnological responses in the central Apennines of Italy. While considering the role of these mechanisms may play a role in the Monte Cristo seismic sequence, it is important to note that in Italy, the responses were studied in high flow karstic aquifers. The two study areas are similar in that they are both present in locations of crustal extension, but different in bedrock geology and climate.

An overarching mechanism identified by the studies in Italy was that hydrologic changes was the largely basin-specific nature of the hydrologic changes. Different basins experienced different responses to earthquakes. This study in Nevada notably has been able to identify how strain played a role in the response within each basin, showing that the hydrologic response has both site-specific features related to the basin hydrogeology as well as those related to the seismic properties, including sign and magnitude of strain.

One mechanism described in the Apennine Mountains studies was crustal degassing. Dissolved gasses, primarily CO_2, have been correlated to seismicity as either fracturing enables its release from deep sources, or seismic events act as a catalyst for increased carbonate dissolution. Carbon isotope signatures in the waters sampled experienced a shift due to this process. Other gasses, both major and trace gasses were found to be escaping along with the CO_2 (Binda et al., 2020). Either dilatational or contractional strain could have played a role here in creating or expanding already existing fractures. The result would be increased porosity allowing for the easier release of the gasses deep in the aquifer. Increased carbonate dissolution may also be a product of shear strain as geologic units may grind together as they move through the

introduction of stress. This may produce more weathering faces and thereby increase the rate of dissolution. The results of the $\delta^{13}C_{DIC}$ were inconclusive and did not span the entire time series, nor were there pre-main shock data. No other gasses were sampled and thus no conclusions can be made about the role of deep-seated gasses.

Another change in groundwater properties reported for earthquakes in the Apennines was aquifer breaching. Here, a change in pore pressure induced fractures in aquitards that separated different waters (Binda et al., 2020). This change in pore pressure can be attributed to contractional stresses. This may have been seen in the inferred upwelling of deep waters in this study, but remains speculative.

Groundwater changes in the Apennines were not always interpreted to be due to external effects of earthquakes. Effects such as internal fracturing have been responsible for groundwater changes observed in the Apennine Mountains. Increased concentrations of chemical components were seen as fresh weathering surfaces were exposed to groundwater leading to increased water-rock interaction. As a result, an increase in porosity and therefore permeability was seen leading to faster flowrates in several instances. The introduction of shaking in karst aquifers was interpreted to have allowed for seepage of highly mineralized pore water in slow-flow circuits to move into faster-flow circuits and alter groundwater quality (Binda et al., 2020). This mechanism also played a key role in the study conducted by Rosen et al., (2018) in the central Apennines, but was not evaluated in this study, as the elemental data remain under investigation.

5. Conclusions and Future Work

The Monte Cristo Earthquake Sequence was the largest seismic sequence in the state of Nevada in the last 70 years. Probable hydrochemical response to this seismicity

was observed in the near and intermediate field, in springs and in wells within a 40km radius.

This study is the first of its kind that I am aware of where the separation of magnitude, strain, and epicenter location were compared to groundwater physiochemical parameters. It is also the first to couple a regional strain analysis with hydrochemical response to a seismic sequence. This study is also distinct from previous work in that seasonal and climate effects were separated from seismic effects on flowrate at one spring and are best attributed to dynamic stress changes during the early part of the seismic sequence.

Changes in groundwater recharge didn't have any recorded effect on physiochemical measurements throughout this study. The only exception to being a possible dilution of the response to the June 30th seismic activity at the Mina Dump due to increased flow during the time of the earthquake.

Dynamic strain in the near field during the early, the most intense part of the sequence may have increased the contribution of source waters derived upgradient in the Columbus Marsh site thereby lowering groundwater isotope signatures and SpC through the unclogging of fractures.

Differential response to two closely spaced events in November and December 2020 is best attributed to a differential in static stress which changed from dilatational to contractional strain at the Columbus Marsh. These static strain changes would have affected pore pressure and may have caused downwelling and later upwelling within a chemically stratified aquifer thereby creating the initial drops and recovery of SpC and pH that were observed. Mixing processes in aquifers appear to be associated with the location of strain relative to the sample location as seen at the Fish Lake Valley following the December 2nd, 2020 event. Increased stress sensed in the upwelling of warmer

waters on October 30th, 2020 may present a precursory signal to seismicity.

Changes in physiochemical parameters are largely related to processes of mixing as a result of strain and are different than the processes attributed to physiochemical changes similar to those recorded in the Italy seismic sequence in 2016-2017. In Italy, expulsion of high solute pore water into fast flow circuits within a karstic aquifer were the major mechanism proposed to explain transient increases in solute concentrations and underscore how regional geology and climate affect hydrochemical response (Rosen et al., 2018).

The aftershock events were comparatively small compared to most notable seismic events and did not cause enough strain to be seen through the MAGNET GPS network. Here it is concluded that while strain may not be detectable through GPS movement, its presence can be inferred through identifying changes in regional groundwater systems.

This study provides the framework for improved methods to better analyze the impacts earthquakes may have on the hydrogeological environment. Work in progress on analysis of the samples taken for elemental chemistry by University of Insubria in Como Italy may help better constrain mechanisms responsible for groundwater response through identifying drivers through changes in SpC, alkalinity, and pH. Further studies of earthquake response paired with a strain analysis in various regions may lead to a more comprehensive understanding of the relationship between strain and groundwater properties within aquifers.

6. References Cited

Abatzoglou, J. T. (2011). Development of gridded surface meteorological data for ecological applications and modelling. *International Journal of Climatology*, *33*(1), 121–131. https://doi.org/10.1002/joc.3413

Albers, J. P., & Stewart, J. H. (1972). *Geology and Mineral Deposits of Esmeralda County, Nevada* (78th ed.). Nevada Bureau of Mines and Geology. https://ngmdb.usgs.gov/Prodesc/proddesc_26323.htm

Angster, S. J., Wesnousky, S. G., Figueiredo, P. M., Owen, L. A., & Hammer, S. J. (2019). Late Quaternary slip rates for faults of the central Walker Lane (Nevada, USA): Spatiotemporal strain release in a strike-slip fault system. *Geosphere*, *15*(5), 1460–1478. https://doi.org/10.1130/GES02088.1

Binda, G., Pozzi, A., Michetti, A. M., Noble, P. J., & Rosen, M. R. (2020). Towards the Understanding of Hydrogeochemical Seismic Responses in Karst Aquifers: A Retrospective Meta-Analysis Focused on the Apennines (Italy). *Minerals*, *10*(12), 1058. https://doi.org/10.3390/min10121058

Brodsky, E. E. (2003). A mechanism for sustained groundwater pressure changes induced by distant earthquakes. *Journal of Geophysical Research*, *108*(B8), 2390. https://doi.org/10.1029/2002JB002321

Crandall-Bear, A., & Hammond, W. C. (2021). *Testing Models of Active Tectonics in the Central Walker Lane Using Satellite Geodetic Measurement of the Mw 6.5 Monte Cristo Range Earthquake*.

Events. (2010). Nevada Seismological Lab. http://www.seismo.unr.edu/Earthquake

Ferguson, H. G., Muller, S. W., & Cathcart, S. H. (1953). *Geologic Map of the Coaldale Quadrangle, Nevada* (GQ-23). USGS.

Hammond, W. C., Blewitt, G., Kreemer, C., Koehler, R. D., & Dee, S. (2021). Geodetic Observation of Seismic Cycles before, during, and after the 2020 Monte Cristo Range, Nevada Earthquake. *Seismological Research Letters*, *92*(2A), 647–662. https://doi.org/10.1785/0220200338

Hanks, T. C., & Kanamori, H. (1979). A moment magnitude scale. *Journal of Geophysical Research*, *84*(B5), 2348. https://doi.org/10.1029/JB084iB05p02348

Harrill, J. R., & Prudic, D. E. (1998). *Aquifer systems in the Great Basin region of Nevada, Utah, and adjacent states; summary report* (Report No. 1409A; Professional Paper). USGS Publications Warehouse. https://doi.org/10.3133/pp1409A

Huntington, J. L., Hegewisch, K. C., Daudert, B., Morton, C. G., Abatzoglou, J. T., McEvoy, D. J., & Erickson, T. (2017). Climate Engine: Cloud Computing and Visualization of Climate and Remote Sensing Data for Advanced Natural Resource Monitoring and Process Understanding. *Bulletin of the American Meteorological Society*, *98*(11), 2397–2410. https://doi.org/10.1175/BAMS-D-15-00324.1

Koehler, R. D., Dee, S., Elliott, A., Hatem, A., Pickering, A., Pierce, I., & Seitz, G. (2021). Field Response and Surface-Rupture Characteristics of the 2020 M 6.5 Monte Cristo Range Earthquake, Central Walker Lane, Nevada. *Seismological Research Letters*, *92*(2A), 823–839. https://doi.org/10.1785/0220200371

Leelaruban, N., Padmanabhan, G., & Oduor, P. (2017). Examining the Relationship between Drought Indices and Groundwater Levels. *Water*, *9*(2), 82. https://doi.org/10.3390/w9020082

Lopes, T. J., & Evetts, D. M. (2004). *Ground-Water Pumpage and Artificial Recharge Estimates for Calendar Year 2000 and Average Annual Natural Recharge and Interbasin Flow by Hydrographic Area, Nevada* (Scientific Investigations Report No. SIR2004-5239; p. 81). USGS.

Manga, M., & Wang, C.-Y. (2015). Earthquake Hydrology. In *Treatise on Geophysics: Vol. Volume 4*. Elsevier Science.

Maurer, D. K., Lopes, T. J., Medina, R. L., & Smith, J. L. (2004). *Hydrogeology and Hydrologic Landscape Regions of Nevada* (Report No. 2004–5131; Scientific Investigations Report). USGS Publications Warehouse. https://doi.org/10.3133/sir20045131

McKee, T. B., Doesken, N. J., & Kleist, J. R. (1993). *THE RELATIONSHIP OF DROUGHT FREQUENCY AND DURATION TO TIME SCALES*. 6.

Okada, Y. (1985). Surface deformation due to shear and tensile faults in a half-space. *Bulletin of the Seismological Society of America*, *75*(4), 1135–1154. https://doi.org/10.1785/BSSA0750041135

Pierce, I. K. D., Wesnousky, S. G., Owen, L. A., Bormann, J. M., Li, X., & Caffee, M. (2020). Accommodation of Plate Motion in an Incipient Strike-Slip System: The Central Walker Lane. *Tectonics*, *40*(2). https://doi.org/10.1029/2019TC005612

Ross, D. (1961). *Geology and mineral deposits of Mineral County, Nevada*. University of Nevada.

Rush, F. Eugene., Katzer, Terry., Nevada., & Geological Survey (U.S.). (1973). *Water-resources appraisal of Fish Lake Valley, Nevada and California*. State of Nevada, Division of Water Resources. //catalog.hathitrust.org/Record/101759819

Sienz, F., Bothe, O., & Fraedrich, K. (2012). Monitoring and quantifying future climate projections of dryness and wetness extremes: SPI bias. *Hydrology and Earth System Sciences*, *16*(7), 2143–2157. https://doi.org/10.5194/hess-16-2143-2012

Spurr, J. E. (1905). *Geology of the Tonopah mining district, Nevada* (Descritive Geology). USGS.

Stagge, J. H., Tallaksen, L. M., Gudmundsson, L., Van Loon, A. F., & Stahl, K. (2015). Candidate Distributions for Climatological Drought Indices (SPI and SPEI). *International Journal of Climatology*, *35*(13), 4027–4040. https://doi.org/10.1002/joc.4267

Thornthwaite, C. W. (1948). An Approach toward a Rational Classification of Climate. *Geographical Review*, *38*(1), 55. https://doi.org/10.2307/210739

U. S. Geological Survey. (1994). *U. S. Geological Survey Water Data for the Nation*. https://doi.org/10.5066/F7P55KJN

U. S. Geological Survey Earthquakes. (2020). https://www.usgs.gov/natural-hazards/earthquake-hazards/earthquakes.

Van Denburgh, A. S., Glancy, P. A., Geological Survey (U.S.), & Nevada. (1970). *Water-resources appraisal of the Columbus Salt Marsh-Soda Spring Valley area, Mineral and Esmeralda Counties, Nevada*. Nevada Dept. of Conservation and Natural Resources, Division of Water Resources.

Vicente-Serrano, S. M., Beguería, S., & López-Moreno, J. I. (2010). A Multiscalar Drought Index Sensitive to Global Warming: The Standardized Precipitation Evapotranspiration Index. *Journal of Climate*, *23*(7), 1696–1718. https://doi.org/10.1175/2009JCLI2909.1

Wells, D., & Coppersmith, K. (1994). New Empirical Relationships among Magnitude, Rupture Length, Rupture Width, Rupture Area, and Surface Displacement. *Bulletin of the Seismological Society of America*, *84*, 974–1002.

7. Tables

	Degrees North	Degrees West
Mina Dump Road spring	38°25'39"	118°04'30"
Willow Ranch	38°07'18"	117°59'26"
Columbus Salt Marsh	37°50'48"	118°05'42"
Fish Lake Valley hot well	37°51'35"	117°59'03"
Garfield Spring	38°20'59"	118°15'40"
Tony Tipton Property	38°20'32"	118°06'10"

Table 1- Coordinates in decimal degrees North and West for the sample locations analyzed in this study. Locations are listed in WGS84

	May 15th	June 30th	November 13th	December 2nd
Mina Dump Road spring	34.75	32.05	34.54	29.17
Willow Ranch	39.71	36.11	41.70	35.32
Columbus Salt Marsh	11.10	4.51	13.21	9.45
Fish Lake Valley hot well	34.66	32.70	36.33	34.91
Garfield Spring	40.00	34.18	-	-
Tony Tipton Property	28.75	24.60	-	-

Table 2- Distance in km from the epicenter of the largest earthquake to occur within each seismic event to each site.

	May 15th	June 30th	November 13th	December 2nd
Mina Dump Road spring	-339	-4.10	-22.8	3.17
Willow Ranch	511	5.84	15.4	8.45
Columbus Salt Marsh	1.20 E4	-220	122	-44.6
Fish Lake Valley hot well	511	4.74	20.6	0.63
Garfield Spring	-673	-8.07	-	-
Tony Tipton Property	-1.21 E3	-11.3	-	-

Table 3- Coseismic strain experienced by each site throughout each event during 2020. Values are reported in nanostrains (i.e., 1E-9 strains). Note that negative values represent contraction whereas positive values represent dilatation.

Event	Date	Magnitude	Fault Length	Depth of Epicenter	Slip Type	Displacement
May						
1	5/15/2020	6.41	17.017	2.70	Normal Oblique	0.977
June						
1	6/30/2020	5.00	1.608	8.30	Right Lateral	0.458
November						
1	11/13/2020	4.30	0.401	10.10	Right Lateral	0.657
2	11/13/2020	4.00	0.221	9.03	Right Lateral	0.767
3	11/13/2020	5.30	2.916	4.80	Right Lateral	0.392
December						
1	12/1/2020	4.30	0.401	5.60	Normal Oblique	0.657
2	12/1/2020	4.30	0.401	4.80	Right Lateral	0.657
3	12/1/2020	5.10	1.961	5.00	Right Lateral	0.435
4	12/2/2020	4.40	0.489	4.10	Right Lateral	0.624
5	12/2/2020	4.30	0.401	4.76	Right Lateral	0.657
6	12/2/2020	4.40	0.489	4.30	Right Lateral	0.624
7	12/3/2020	4.90	1.318	5.00	Right Lateral	0.482

Table 4- Modeled fault parameters for all seismic aftershock events > M_w 4. Fault length and depth of epicenter are displayed in kilometers (km), magnitude is represented in moment magnitude (Mw), and displacement is in meters.

Climate Category	SPEI Values	Probability %
Severely Wet	2.00 to 1.50	4.4
Moderately Wet	1.00 to 1.49	9.2
Mildly Wet	0.1 to 0.99	68.2
Normal Conditions	0	
Mild Drought	-0.1 to -0.99	
Moderate Drought	-1.00 to -1.49	9.2
Severe Drought	-1.50 to 2.00	4.4

Table 5- The probability and description of various SPEI value ranges.

8. Figures

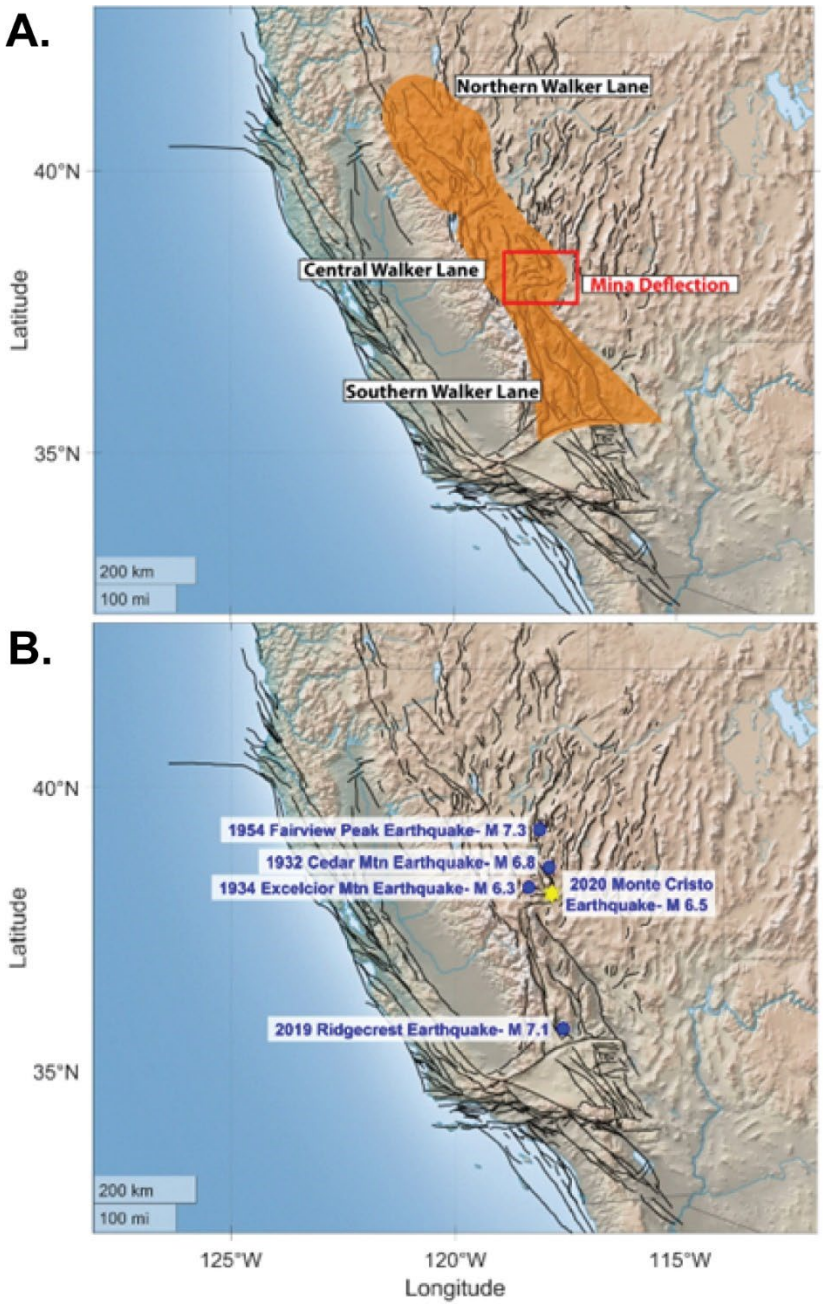

Figure 1- (A) Map of the Walker Lane and the Mina Deflection. (B) Map showing historical seismic events and the M 6.5 Monte Cristo event. On both maps faults are represented by thick black lines.

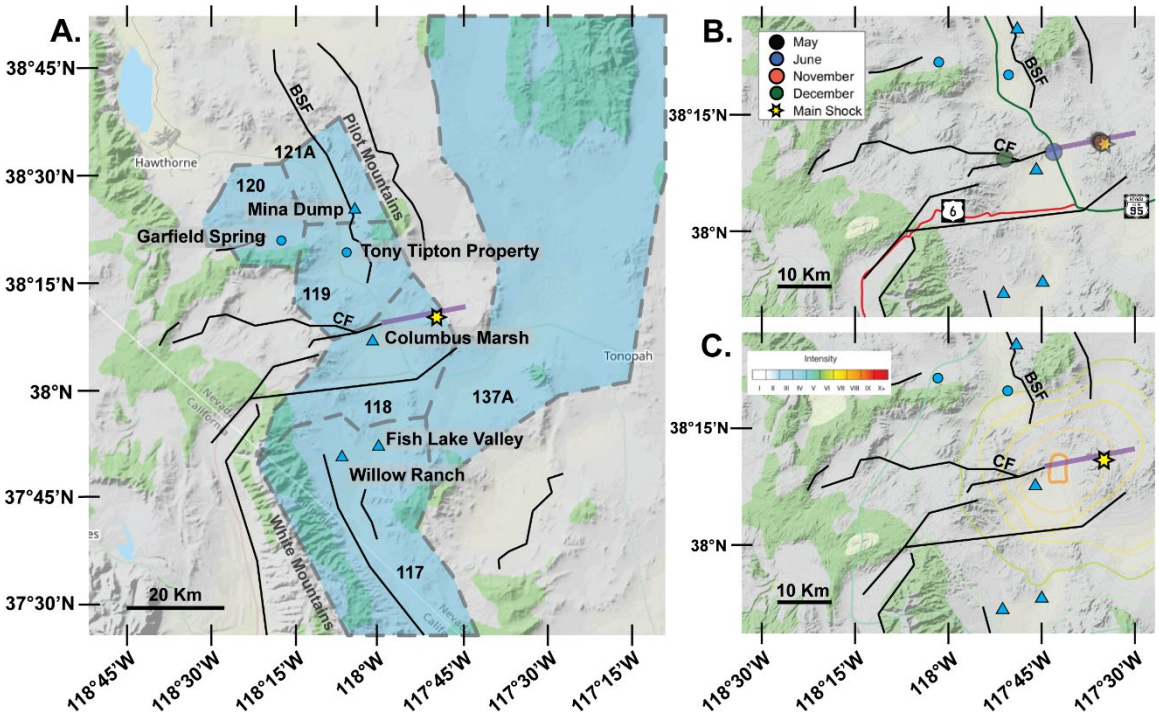

Figure 2 - Regional Map of major faults surrounding the location of the Monte Cristo Seismic Sequence. The locations of sample sites and other points of interest are also provided. (A) Regional Map with hydrographic basins delineated and labeled accordingly. (B) The largest aftershocks of each sequence are provided. (C) The seismic intensity map showing the distribution of intensity as a result of the main M 6.5 shock. Earthquake data provided by the USGS (*U. S. Geological Survey Earthquakes*, 2020).

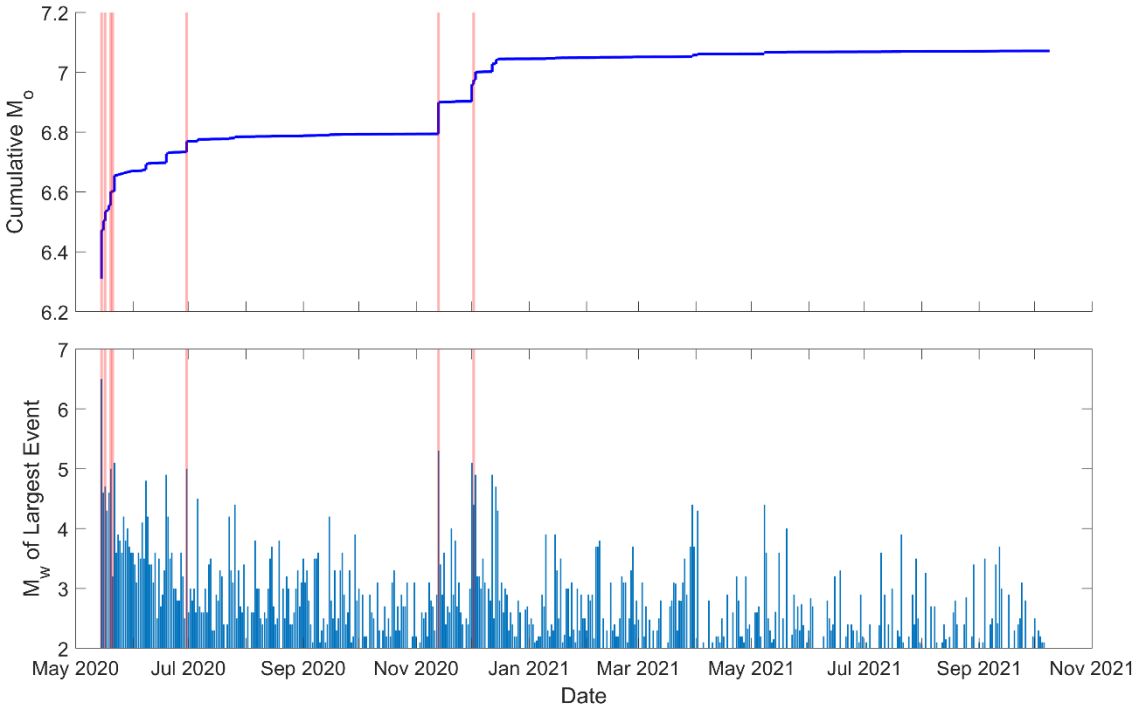

Figure 3 - Graph representing the total cumulative magnitude of the Monte Cristo Seismic Sequence following the main M 6.5 shock.

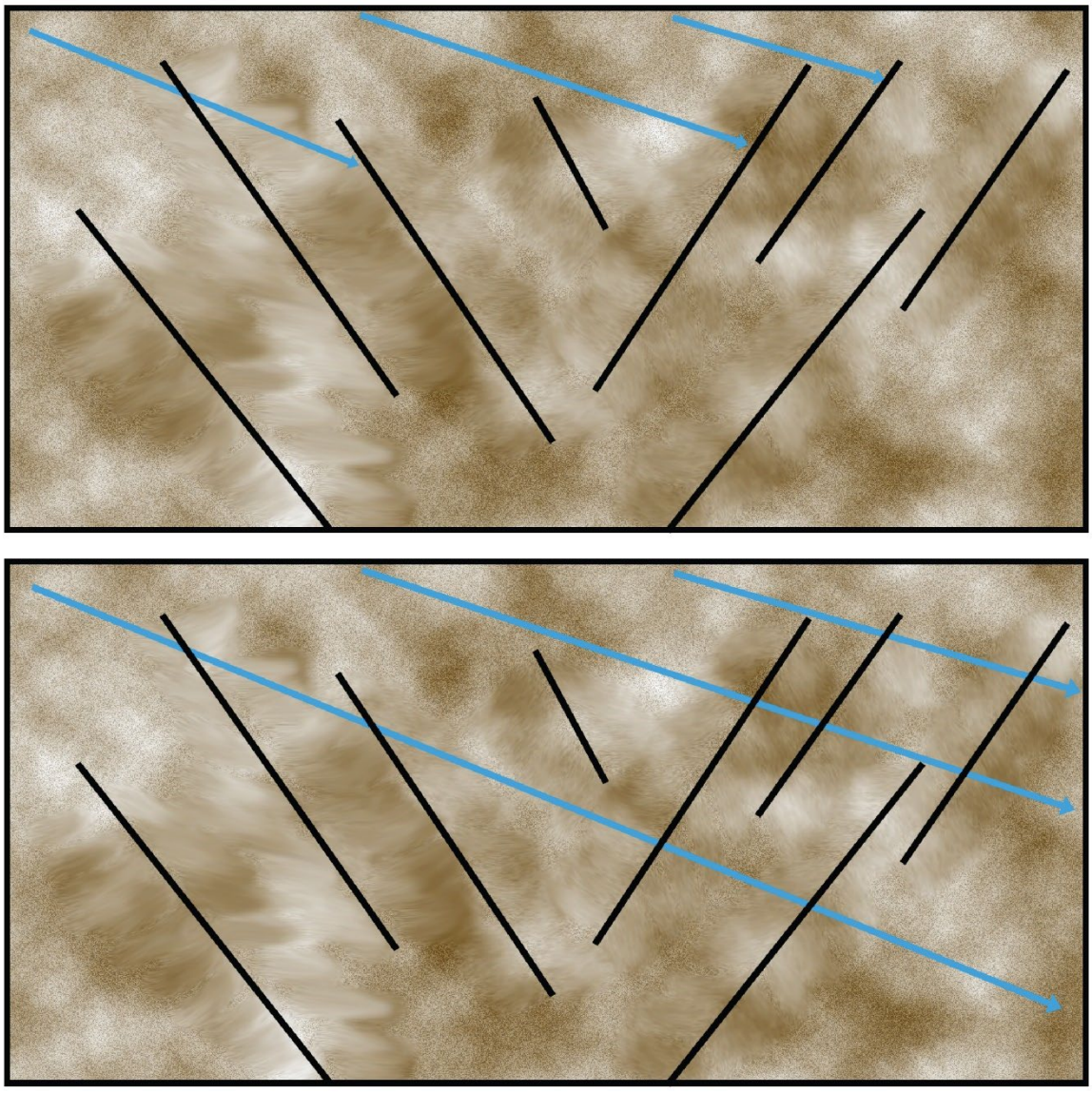

Figure 4 - (top) General schematic of clogged fractures (black lines) prohibiting flow (blue lines). (bottom) unclogged fractures allowing flow to pass through.

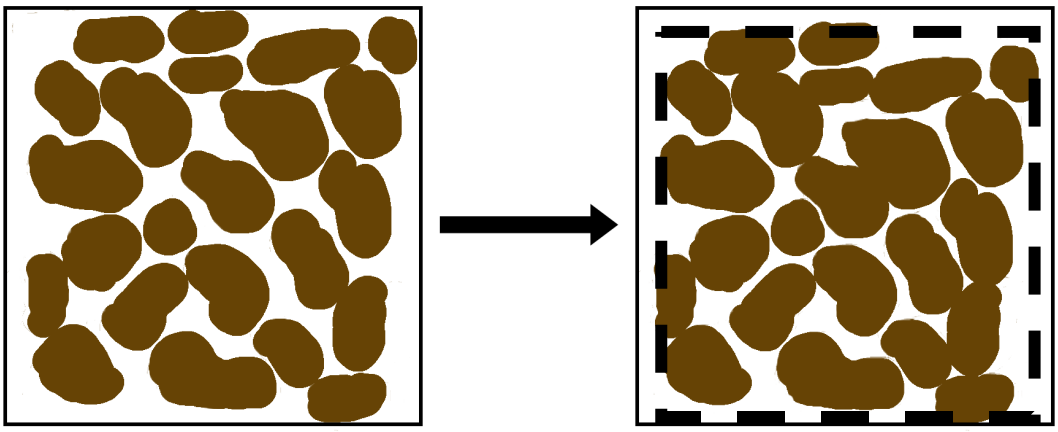

Figure 5 - Schematic showing consolidation of loose sediments.

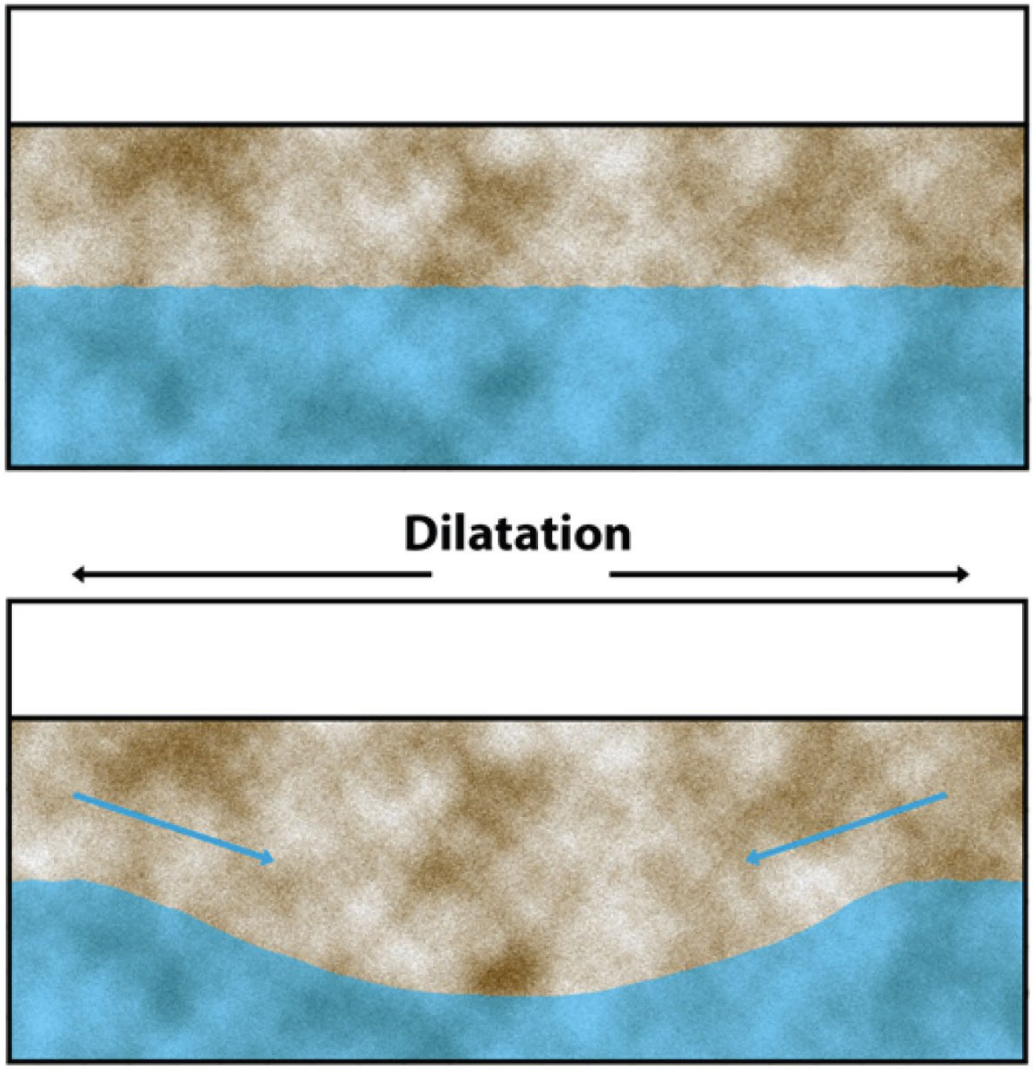

Figure 6 - Schematic representing the change in groundwater level as a result of dilatational static strain. The black lines above the bottom diagram represent the direction of strain. The blue lines represent the direction of flow of groundwater.

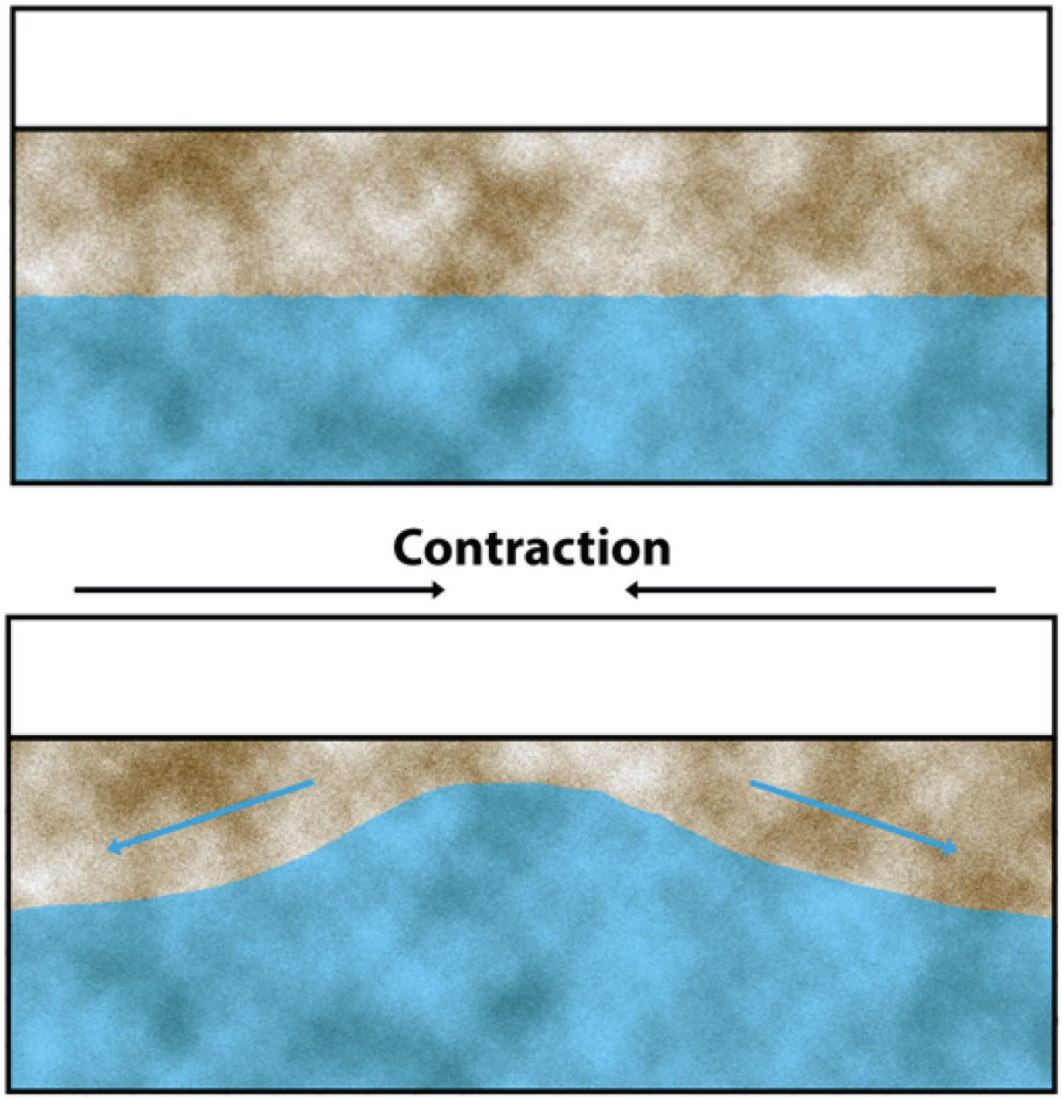

Figure 7 - Schematic representing the change in groundwater level as a result of contractional static strain. The black lines above the bottom diagram represent the direction of strain. The blue lines represent the direction of flow of groundwater.

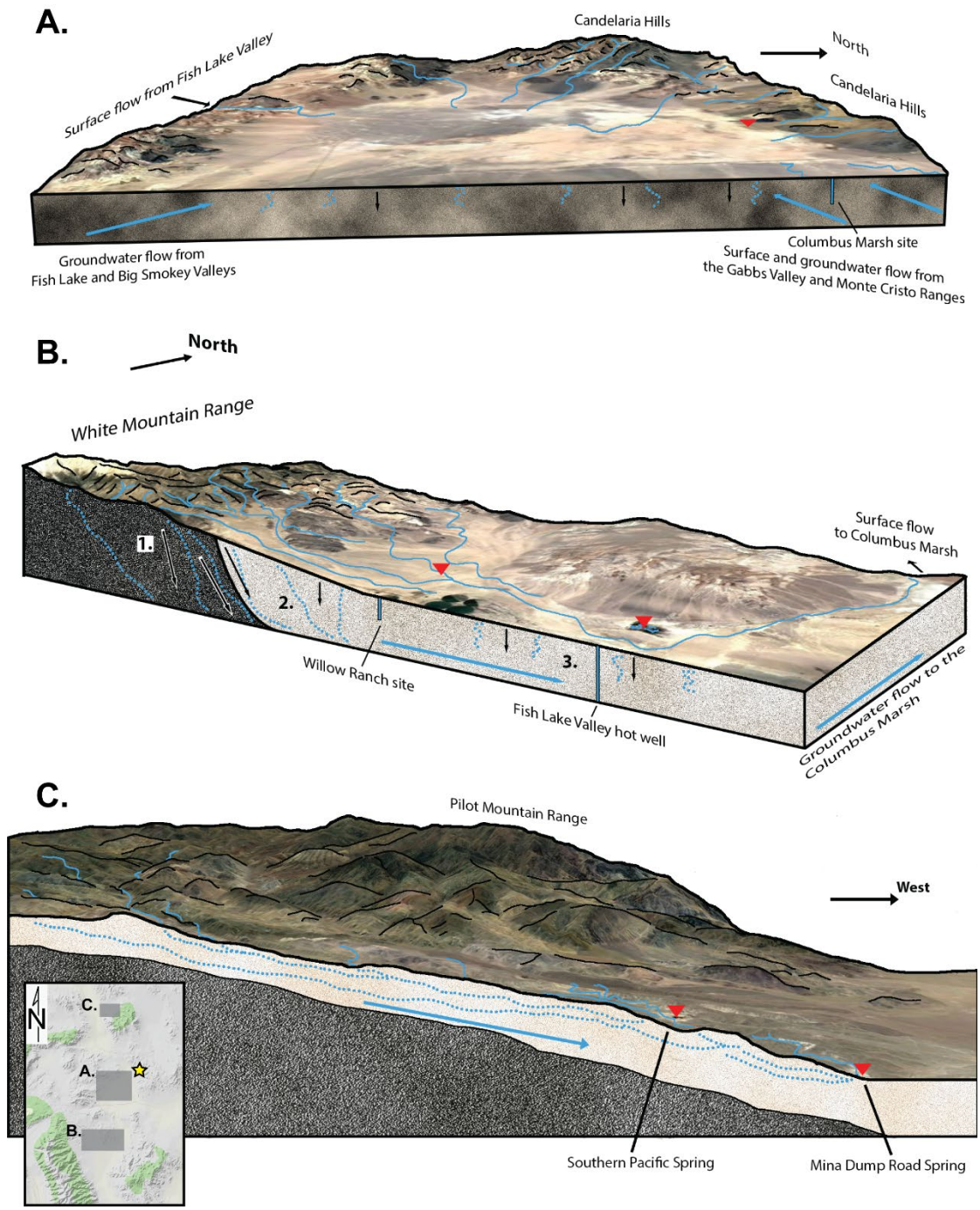

Figure 8 - Conceptual recharge model of flow paths responsible for recharge within the (A) Columbus Marsh Hydrographic Basin, (B) Fish Lake Valley Hydrographic Basin and (C) Eastern Soda Springs Hydrographic Basin. Sample locations and nearby springs are shown with red arrows. Wells are projected on the side of the cross section. Blue lines represent flow paths, dotted blue lines represent the subsurface flow paths. The primary recharge processes are shown with black arrows and are labeled with numbers. A locality map is provided at the bottom left of the figure with the cutouts labeled accordingly. The yellow star represents the epicenter of the main M 6.5 shock.

Figure 9 - Photo of the Columbus Marsh site looking south on April 3rd, 2021. Water is pumped from the shed, and is fed through the depot outlet to the right.

Figure 10 - Photo of the Fish Lake Valley hot well looking east on May 23rd, 2020. Forrest (left) and Nadine Fasig (right) testing the flow rate of the artesian well.

Figure 11 - Photo of the Mina Dump Road spring looking northeast on October 8th, 2021.

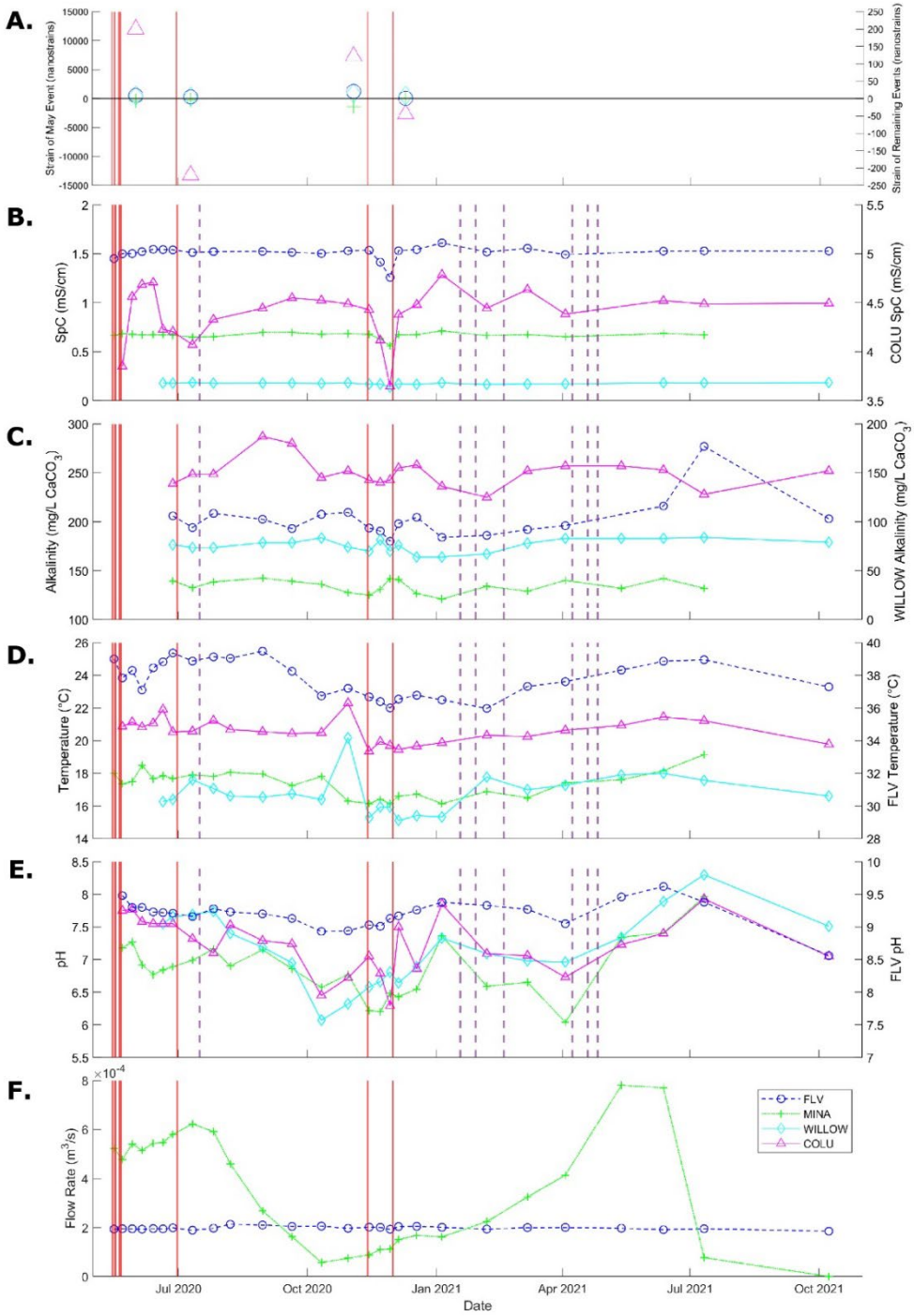

Figure 12 – Time series plots of (A) Sign and magnitude of strain at each sampling location (B) specific conductance (SpC), from the Fish Lake Valley hot well (FLV), the Mina Dump Road spring (MINA), the Willow Ranch site (WILLOW), and the Columbus Marsh (COLU). (C) of Alkalinity (mg/L as $CaCO_3$), (D) of Temperature (°C), (E) of pH, and (F) of flow rate (m^3/s). Red vertical lines represent seismic events >M_w 5 (shocks on and in the days following May 15th, 2020, June 30th, 2020, November 13th, 2020, and December 2nd, 2020). Purple dashed vertical lines represent times where pumping took place at the COLU site.

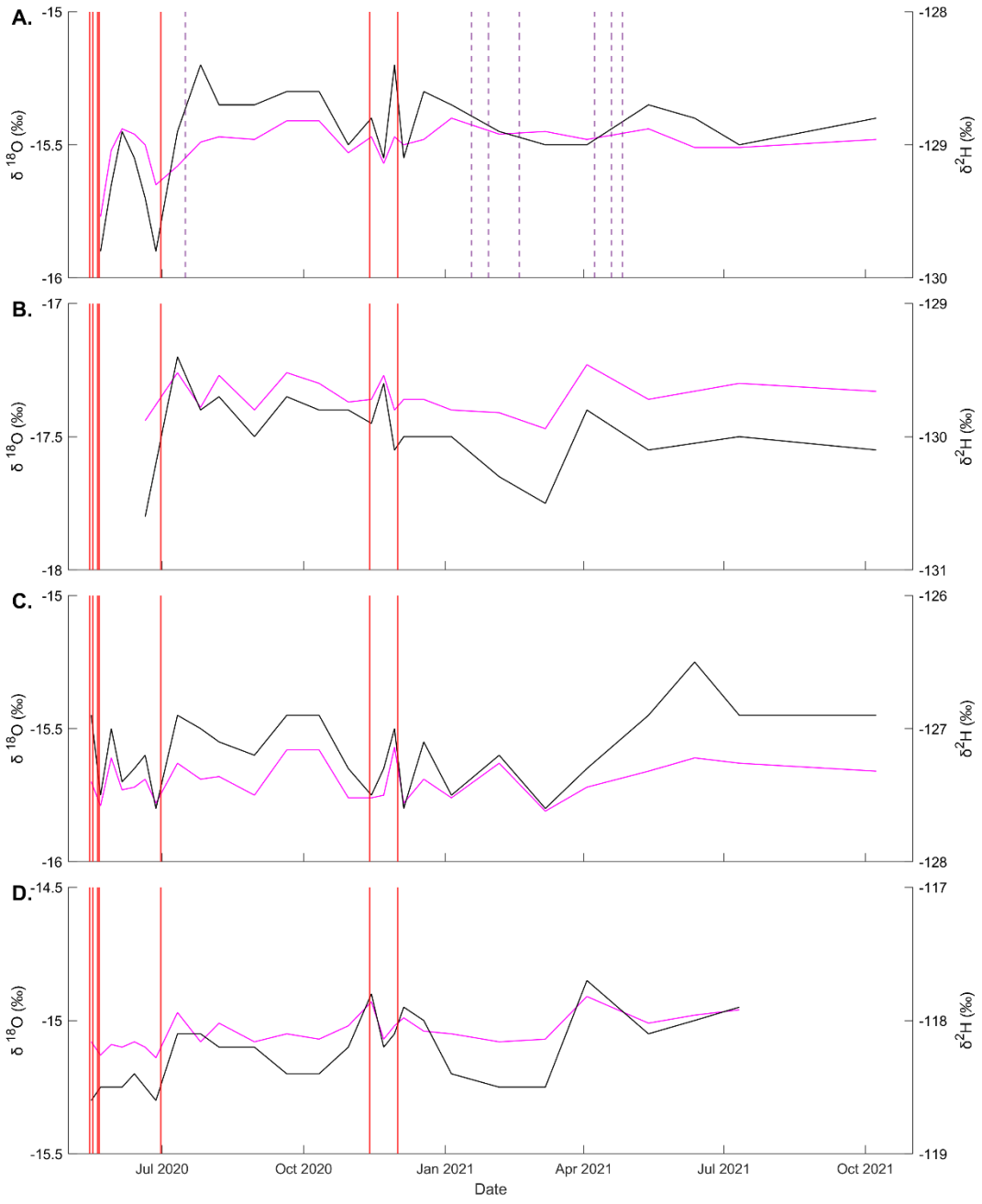

Figure 13 - Isotope plots of (A) the Columbus Marsh, (B) the Willow Ranch (C) the Fish Lake Valley hot well (D) the Mina Dump Road spring. $\delta^{18}O$ is represented in magenta on the left axis and $\delta^{2}H$ is represented in black on the right axis. Vertical red lines represent seismicity > M 5.

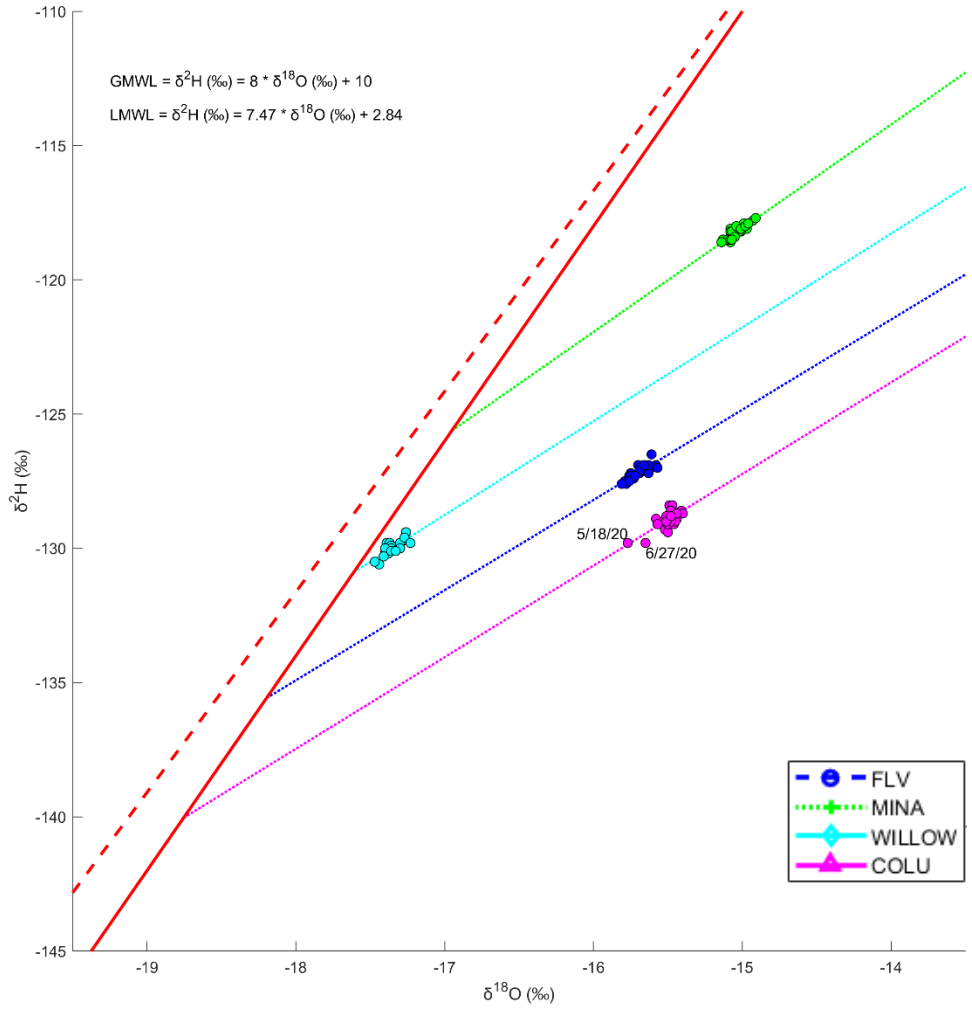

Figure 14 – Groundwater isotopes of all sampling locations. The Global Meteoric Water Line (GMWL) is represented by the solid red line and the Local Meteoric Water Line (LMWL) is represented with dashed red line. Evaporation lines are provided by site. Isotope samples of interest are noted with labels of their collection date. The GMWL is provided by Craig (1961) and the LMWL is provided by Lachniet et al. (2020). The equation for the trendline of FLV is $\delta^2H=3.36*\delta^{18}O-74.45$ with an R^2 value of 0.71. The equation for the trendline of MINA is $\delta^2H=3.86*\delta^{18}O-60.14$ with an R^2 value of 0.78. The equation for the trendline of WILLOW is $\delta^2H=3.49*\delta^{18}O-69.39$ with an R^2 value of 0.64. The equation for the trendline of COLU is $\delta^2H=3.41*\delta^{18}O-76.06$ with an R^2 value of 0.56.

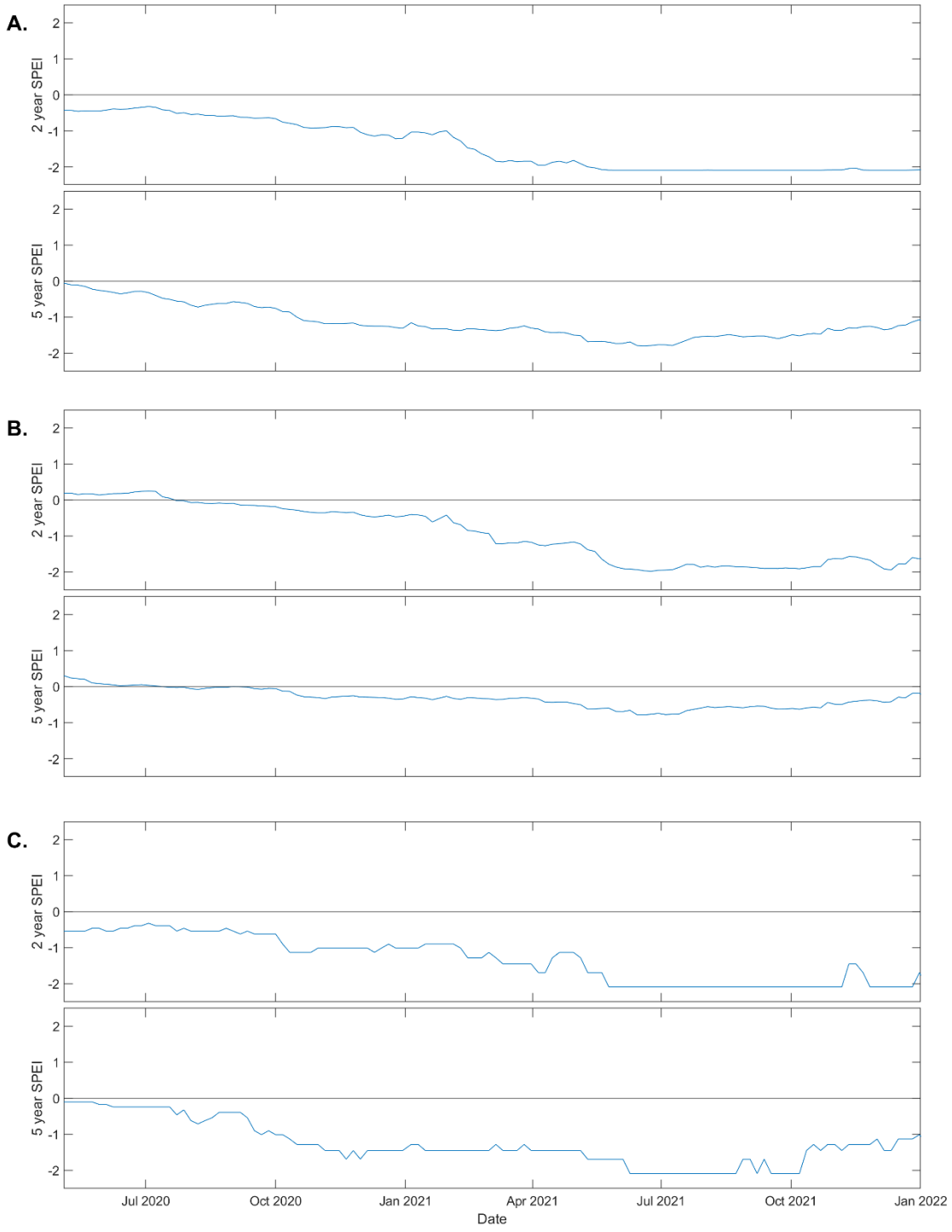

Figure 15 – SPEI analysis of (A) Columbus Marsh Hydrographic Basin (number 118), (B) Fish Lake Valley Hydrographic Basin (number 117), and (C) Eastern Soda Spring Hydrographic Basin (number 121A). For each basin, the 2-year

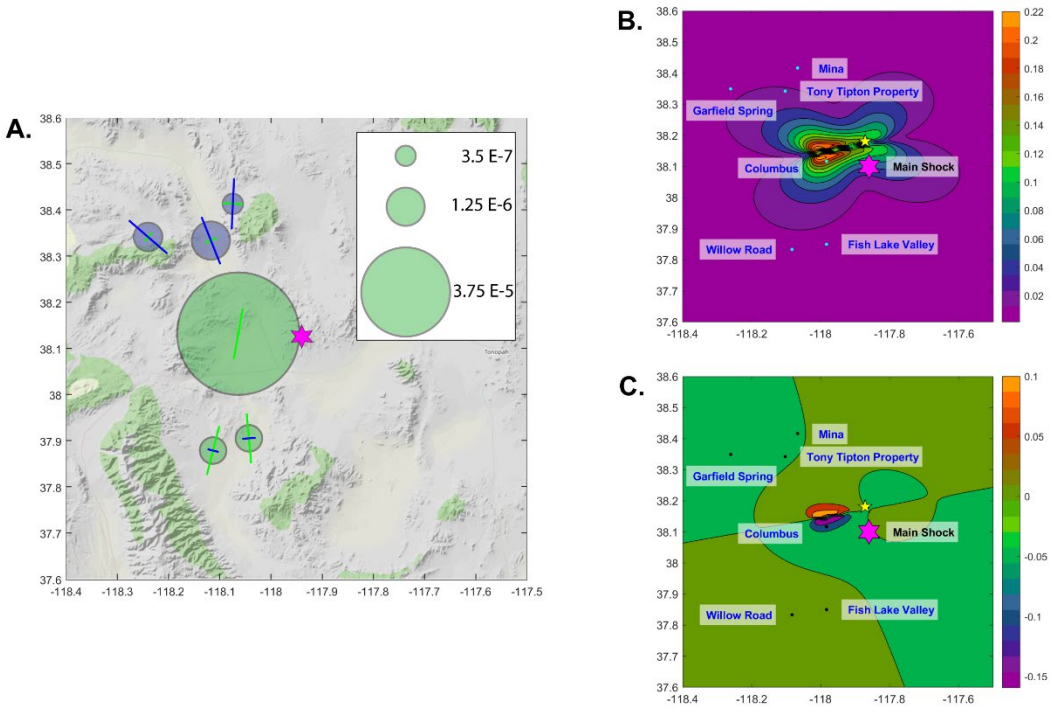

Figure 16 - Strain analysis for the May 15th M 6.5 event. On subfigures B and C events > M 4 are represented with yellow stars and on all subfigures the M 6.5 event is represented with a purple hexagram. (A) Plot of normalized strain tensors showing modeled strain experienced by each site as a result of seismicity. Green axes represent extension and blue axes represent contraction. Circles plotted on each site represent the magnitude of strain each site experienced. Green circles represent dilatational strain, and blue circles represent contractional strain. (B) Contour map of modeled horizontal displacement with displacement units in cm. (C) Contour map of modeled vertical displacement with displacement units in cm.

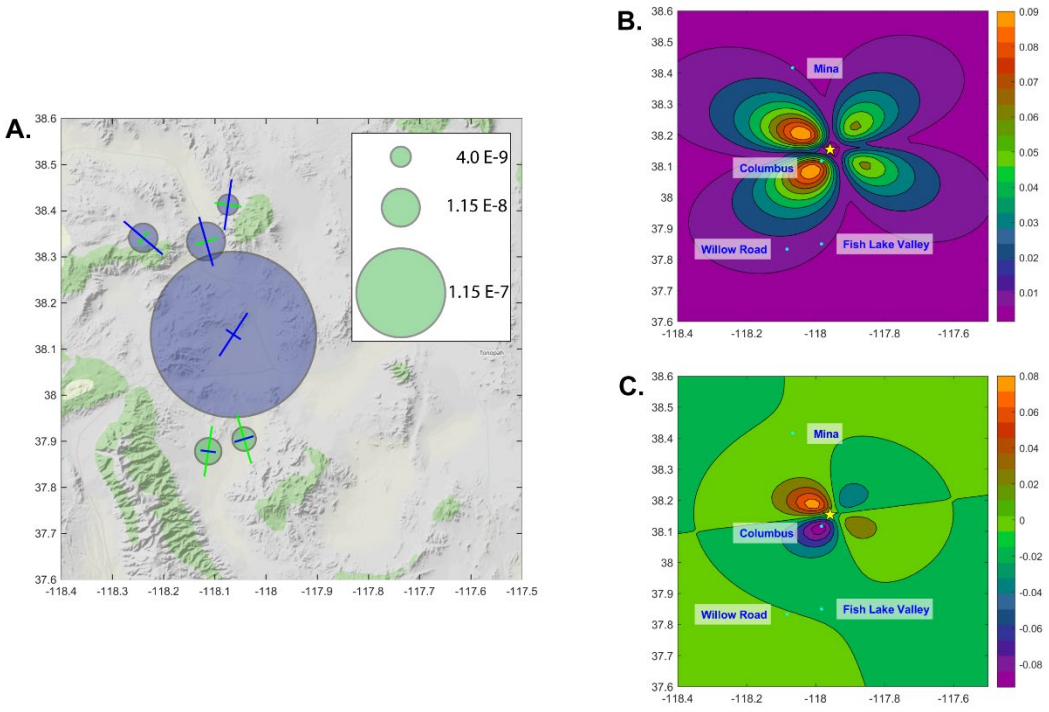

Figure 17 - Strain analysis for the June 30th event. On subfigures B and C events > M 4 are represented with yellow stars. (A) Plot of normalized strain tensors showing modeled strain experienced by each site as a result of seismicity. Green axes represent extension and blue axes represent contraction. Circles plotted on each site represent the magnitude of strain each site experienced. Green circles represent dilatational strain, and blue circles represent contractional strain. (B) Contour map of modeled horizontal displacement with displacement units in cm. (C) Contour map of modeled vertical displacement with displacement units in cm.

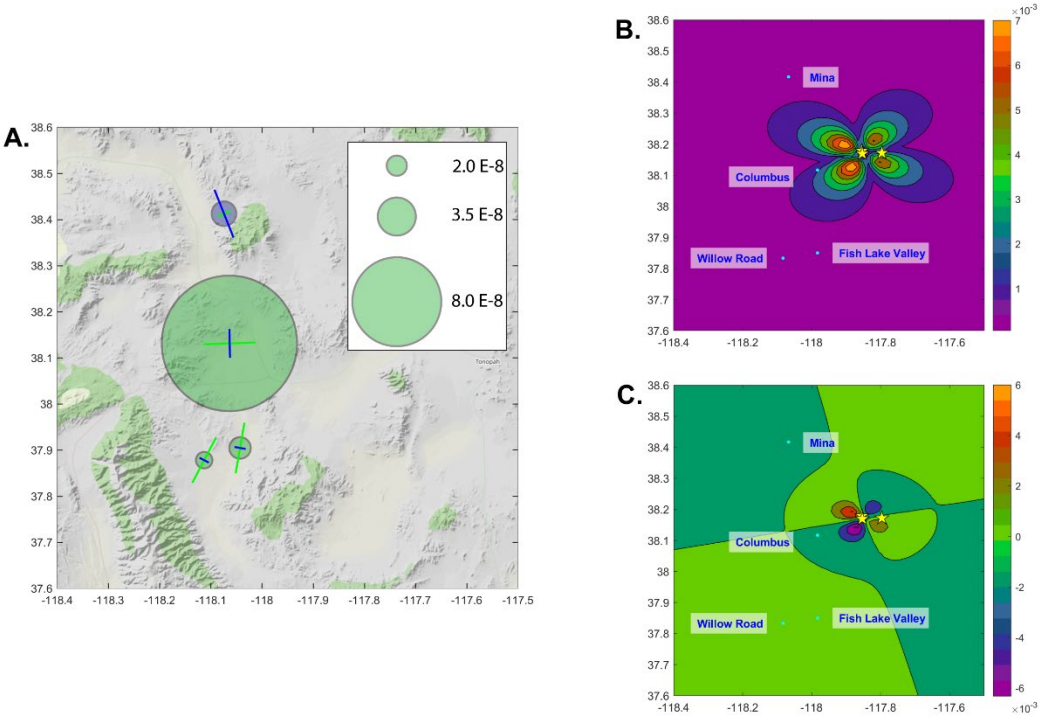

Figure 18 - Strain analysis for the November 13th event. On subfigures B and C events > M 4 are represented with yellow stars. (A) Plot of normalized strain tensors showing modeled strain experienced by each site as a result of seismicity. Green axes represent extension and blue axes represent contraction. Circles plotted on each site represent the magnitude of strain each site experienced. Green circles represent dilatational strain, and blue circles represent contractional strain. (B) Contour map of modeled horizontal displacement with displacement units in cm. (C) Contour map of modeled vertical displacement with displacement units in cm.

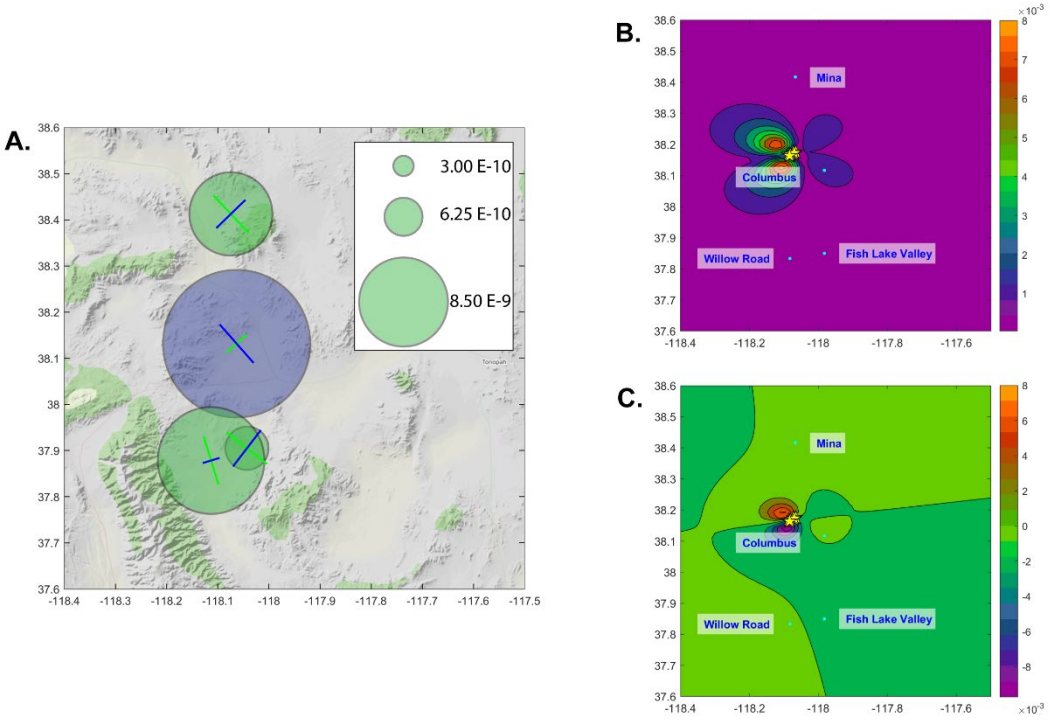

Figure 19 - Strain analysis for the December 2nd event. On subfigures B and C events > M 4 are represented with yellow stars. (A) Plot of normalized strain tensors showing modeled strain experienced by each site as a result of seismicity. Green axes represent extension and blue axes represent contraction. Circles plotted on each site represent the magnitude of strain each site experienced. Green circles represent dilatational strain, and blue circles represent contractional strain. (B) Contour map of modeled horizontal displacement with displacement units in cm. (C) Contour map of modeled vertical displacement with displacement units in cm.

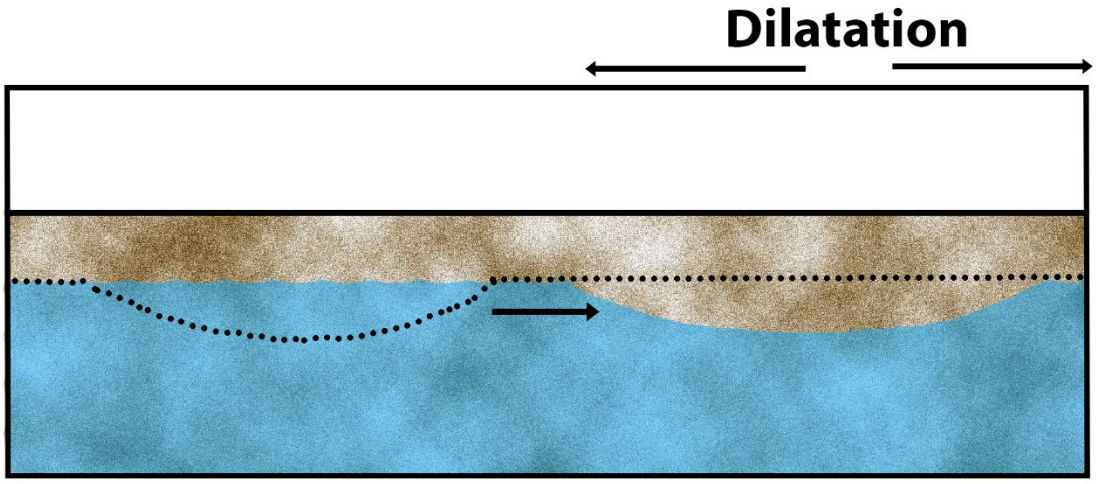

Figure 20 - Schematic representing the change in location of groundwater mixing as a result of a change in location of dilatational static strain. The black dotted line represents the previous groundwater contour and the black arrow on the diagram shows the direction of movement of the groundwater contours as a result of dilatation.

9. Appendices

Specific Conductance (mS/cm)					
Date	FISH LAKE VLY HOT WELL	MINA DUMP ROAD	COLUMBUS MARSH DEPOT	WILLOW ROAD RANCH	GAP SPRING
5/16/2020	1.451	0.666			
5/22/2020	1.500	0.685	3.852		10.710
5/29/2020	1.502	0.679	4.563		
6/5/2020	1.522	0.673	4.687		
6/13/2020	1.546	0.677	4.706		
6/20/2020	1.543	0.675	4.227	0.18	
6/27/2020	1.54	0.668	4.206	0.179	
7/11/2020	1.513	0.651	4.072	0.187	
7/26/2020	1.522	0.654	4.329	0.179	12.300
8/7/2020					
8/30/2020	1.524	0.697	4.444	0.18	
9/20/2020	1.515	0.697	4.55	0.18	
10/11/2020	1.503	0.68	4.525	0.178	
10/30/2020	1.53	0.684	4.488	0.182	
11/14/2020	1.536	0.678	4.429	0.171	
11/22/2020	1.414	0.633	4.116	0.17	
11/29/2020	1.259	0.559	3.647	0.141	
12/5/2020	1.531	0.674	4.379	0.173	
12/18/2020	1.543	0.677	4.481	0.169	
1/5/2021	1.611	0.712	4.786	0.182	
2/6/2021	1.518	0.665	4.445	0.168	
3/7/2021	1.556	0.676	4.635	0.172	
4/3/2021	1.491	0.653	4.385	0.173	
5/13/2021					
6/12/2021	1.527	0.687	4.522	0.184	
7/11/2021	1.529	0.673	4.488	0.182	
10/8/2021	1.528		4.494	0.185	
12/8/2021					

Appendix 1- Specific conductance data by site. Data provided in mS/cm.

Alkalinity (mg/L $CaCO_3$)				
Date	FISH LAKE VLY HOT WELL	MINA DUMP ROAD	COLUMBUS MARSH DEPOT	WILLOW ROAD RANCH
5/16/2020				
5/22/2020				
5/29/2020				
6/5/2020				
6/13/2020				
6/20/2020				
6/27/2020	206	140	239	76.5
7/11/2020	194	133	249	74
7/26/2020	209	139	249	74
8/7/2020				
8/30/2020	203	143	287	79
9/20/2020	193	139	280	79
10/11/2020	208	136	245	84
10/30/2020	210	128	252	74
11/14/2020	194	125	243	70
11/22/2020	191	131	240	82
11/29/2020	180	142	243	70
12/5/2020	198	141	255	76
12/18/2020	205	127	258	64
1/5/2021	184	121	236	64
2/6/2021	186	134	225	67
3/7/2021	192	129	252	78
4/3/2021	196	140	257	83
5/13/2021		132	257	83
6/12/2021	216	142	253	83
7/11/2021	277	132	228	84
10/8/2021	203		252	79
12/8/2021				

Appendix 2- Alkalinity data by site. Data provided in mg/L CaCO3.

Temperature				
Date	FISH LAKE VLY HOT WELL	MINA DUMP ROAD	COLUMBUS MARSH DEPOT	WILLOW ROAD RANCH
5/16/2020	39.00	18.00		
5/22/2020	37.84	17.36	20.86	
5/29/2020	38.30	17.48	21.14	
6/5/2020	37.10	18.49	20.83	
6/13/2020	38.46	17.65	21.07	
6/20/2020	38.82	17.84	21.91	16.27
6/27/2020	39.37	17.68	20.53	16.40
7/11/2020	38.87	17.90	20.58	17.60
7/26/2020	39.13	17.81	21.24	17.07
8/7/2020	39.04	18.06	20.68	16.60
8/30/2020	39.48	17.95	20.55	16.54
9/20/2020	38.25	17.25	20.43	16.75
10/11/2020	36.74	17.80	20.49	16.39
10/30/2020	37.20	16.30	22.30	20.17
11/14/2020	36.68	16.16	19.34	15.28
11/22/2020	36.39	16.40	19.94	15.94
11/29/2020	36.00	16.15	19.70	15.93
12/5/2020	36.54	16.60	19.46	15.11
12/18/2020	36.78	16.72	19.66	15.41
1/5/2021	36.49	16.15	19.87	15.33
2/6/2021	35.97	16.89	20.32	17.77
3/7/2021	37.32	16.50	20.25	17.00
4/3/2021	37.61	17.42	20.64	17.27
5/13/2021	38.32	17.60	20.93	17.91
6/12/2021	38.86	18.16	21.45	18.00
7/11/2021	38.95	19.15	21.22	17.57
10/8/2021	37.29		19.78	16.61
12/8/2021	37.50		20.50	16.00

Appendix 3- Temperature data by site. Data provided in degrees Celsius (°C). The dates highlighted in peach represent dates where a mercury thermometer was the only method of measurement.

pH				
Date	FISH LAKE VLY HOT WELL	MINA DUMP ROAD	COLUMBUS MARSH DEPOT	WILLOW ROAD RANCH
5/16/2020				
5/22/2020	7.98	7.18	7.75	
5/29/2020	7.80	7.27	7.77	
6/5/2020	7.80	6.92	7.58	
6/13/2020	7.73	6.77	7.55	
6/20/2020	7.72	6.84	7.55	7.55
6/27/2020	7.71	6.89	7.55	7.66
7/11/2020	7.66	6.99	7.32	7.69
7/26/2020	7.78	7.16	7.10	7.74
8/7/2020	7.73	6.90	7.53	7.40
8/30/2020	7.70	7.15	7.29	7.19
9/20/2020	7.63	6.86	7.24	6.95
10/11/2020	7.43	6.57	6.45	6.07
10/30/2020	7.44	6.77	6.72	6.32
11/14/2020	7.53	6.22	7.05	6.58
11/22/2020	7.51	6.20	6.79	6.66
11/29/2020	7.63	6.48	6.29	6.81
12/5/2020	7.67	6.43	7.50	6.64
12/18/2020	7.76	6.55	6.86	6.89
1/5/2021	7.88	7.36	7.85	7.33
2/6/2021	7.83	6.59	7.09	7.09
3/7/2021	7.77	6.65	7.06	6.98
4/3/2021	7.55	6.04	6.73	6.96
5/13/2021	7.96	7.34	7.23	7.34
6/12/2021	8.12	7.41	7.40	7.89
7/11/2021	7.88	7.96	7.93	8.30
10/8/2021	7.06		7.05	7.51
12/8/2021				

Appendix 4- pH data by site. The date highlighted in red represents when the pH sensor was not operating properly.

Flow Rate (m^3/s)		
Date	FISH LAKE VLY HOT WELL	MINA DUMP ROAD
5/16/2020	1.9E-04	5.2E-04
5/22/2020	2.0E-04	4.8E-04
5/29/2020	1.9E-04	5.4E-04
6/5/2020	1.9E-04	5.2E-04
6/13/2020	2.0E-04	5.4E-04
6/20/2020	1.9E-04	5.5E-04
6/27/2020	2.0E-04	5.8E-04
7/11/2020	1.9E-04	6.2E-04
7/26/2020	2.0E-04	5.9E-04
8/7/2020	2.1E-04	4.6E-04
8/30/2020	2.1E-04	2.7E-04
9/20/2020	2.0E-04	1.6E-04
10/11/2020	2.1E-04	5.7E-05
10/30/2020	2.0E-04	7.4E-05
11/14/2020	2.0E-04	8.9E-05
11/22/2020	2.0E-04	1.1E-04
11/29/2020	1.9E-04	1.1E-04
12/5/2020	2.0E-04	1.5E-04
12/18/2020	2.0E-04	1.7E-04
1/5/2021	2.0E-04	1.6E-04
2/6/2021	1.9E-04	2.2E-04
3/7/2021	2.0E-04	3.2E-04
4/3/2021	2.0E-04	4.1E-04
5/13/2021	2.0E-04	7.8E-04
6/12/2021	1.9E-04	7.7E-04
7/11/2021	2.0E-04	7.7E-05
10/8/2021	1.9E-04	N/A
12/8/2021	1.9E-04	N/A

Appendix 5- Flow rate data by site. Data provided in cubic meters per second.

‰ $\delta^{13}C_{DIC}$			
Site	Date	Replicate #	‰ $\delta^{13}C_{DIC}$
MINA DUMP ROAD	5/16/2020		-9.6
MINA DUMP ROAD	6/20/2020		-9.3
MINA DUMP ROAD	6/27/2020		-9.7
MINA DUMP ROAD	7/11/2020		-8.57
MINA DUMP ROAD	7/26/2020	rep1	-8.47
MINA DUMP ROAD	7/26/2020	rep2	-8.29
MINA DUMP ROAD	8/7/2020		-8.42
MINA DUMP ROAD	8/30/2020		-8.91
MINA DUMP ROAD	10/11/2020		-8.66
MINA DUMP ROAD	10/30/2020		-9.33
MINA DUMP ROAD	11/14/2020		-9.08
MINA DUMP ROAD	11/22/2020		-8.97
MINA DUMP ROAD	11/29/2020		-9.10
MINA DUMP ROAD	12/5/2020		-8.89
FISH LAKE VLY HOT WELL	6/20/2020		-5.1
FISH LAKE VLY HOT WELL	6/27/2020		-4.9
FISH LAKE VLY HOT WELL	7/11/2020		-4.60
FISH LAKE VLY HOT WELL	7/26/2020		-4.71
FISH LAKE VLY HOT WELL	8/7/2020		-4.14
FISH LAKE VLY HOT WELL	8/30/2020		-4.43
FISH LAKE VLY HOT WELL	9/20/2020	rep1	-5.06
FISH LAKE VLY HOT WELL	9/20/2020	rep2	-4.97
FISH LAKE VLY HOT WELL	10/11/2020		-4.33
FISH LAKE VLY HOT WELL	10/30/2020		-4.36
FISH LAKE VLY HOT WELL	11/14/2020		-4.47
FISH LAKE VLY HOT WELL	11/22/2020	rep1	-4.54
FISH LAKE VLY HOT WELL	11/22/2020	rep2	-4.44
FISH LAKE VLY HOT WELL	11/29/2020		-4.34
FISH LAKE VLY HOT WELL	12/5/2020		-4.66
COLUMBUS MARSH DEPOT	6/20/2020		-8.1
COLUMBUS MARSH DEPOT	6/27/2020		-8.1
COLUMBUS MARSH DEPOT	7/11/2020		-7.34
COLUMBUS MARSH DEPOT	7/26/2020	rep1	-6.77
COLUMBUS MARSH DEPOT	7/26/2020	rep2	-6.99

COLUMBUS MARSH DEPOT	8/7/2020		-7.05
COLUMBUS MARSH DEPOT	8/30/2020		-6.84
COLUMBUS MARSH DEPOT	9/20/2020		-7.18
COLUMBUS MARSH DEPOT	10/11/2020		-7.06
COLUMBUS MARSH DEPOT	10/30/2020		-7.23
COLUMBUS MARSH DEPOT	11/14/2020		-8.49
COLUMBUS MARSH DEPOT	11/22/2020	rep1	-7.56
COLUMBUS MARSH DEPOT	11/22/2020	rep2	-7.51
COLUMBUS MARSH DEPOT	11/29/2020		-7.79
COLUMBUS MARSH DEPOT	12/5/2020		-7.48
WILLOW ROAD RANCH	6/20/2020		-11.6
WILLOW ROAD RANCH	6/27/2020		-11.3
WILLOW ROAD RANCH	7/11/2020	rep1	-10.01
WILLOW ROAD RANCH	7/11/2020	rep2	-10.00
WILLOW ROAD RANCH	7/20/2020		-11.29
WILLOW ROAD RANCH	7/26/2020		-9.90
WILLOW ROAD RANCH	8/7/2020		-10.23
WILLOW ROAD RANCH	8/30/2020		-10.13
WILLOW ROAD RANCH	10/11/2020		-9.85
WILLOW ROAD RANCH	10/30/2020		-10.47
WILLOW ROAD RANCH	11/14/2020	rep1	-11.80
WILLOW ROAD RANCH	11/14/2020	rep2	-12.17
WILLOW ROAD RANCH	11/22/2020		-10.99
WILLOW ROAD RANCH	11/29/2020		-12.32
WILLOW ROAD RANCH	12/5/2020		-11.11
GARFIELD	7/28/2020		-11.84

Appendix 6- Dissolved inorganic carbon ($\delta^{13}C_{DIC}$) data listed by site.

Groundwater Isotopes			
Site	Date	‰ $\delta^{18}O$	‰ $\delta^{2}H$
MINA DUMP ROAD	5/16/2020	-15.08	-118.60
MINA DUMP ROAD	5/22/2020	-15.13	-118.50
MINA DUMP ROAD	5/22/2020	-14.68	-115.70
MINA DUMP ROAD	5/29/2020	-15.09	-118.50
MINA DUMP ROAD	6/5/2020	-15.10	-118.50
MINA DUMP ROAD	6/13/2020	-15.08	-118.40
MINA DUMP ROAD	6/20/2020	-15.10	-118.50
MINA DUMP ROAD	6/27/2020	-15.14	-118.60
MINA DUMP ROAD	7/11/2020	-14.97	-118.10
MINA DUMP ROAD	7/26/2020	-15.08	-118.10
MINA DUMP ROAD	8/7/2020	-15.01	-118.20
MINA DUMP ROAD	8/30/2020	-15.08	-118.20
MINA DUMP ROAD	9/20/2020	-15.05	-118.40
MINA DUMP ROAD	10/11/2020	-15.07	-118.40
MINA DUMP ROAD	10/30/2020	-15.02	-118.20
MINA DUMP ROAD	11/14/2020	-14.93	-117.80
MINA DUMP ROAD	11/22/2020	-15.07	-118.20
MINA DUMP ROAD	11/29/2020	-15.02	-118.10
MINA DUMP ROAD	12/5/2020	-14.99	-117.90
MINA DUMP ROAD	12/18/2020	-15.04	-118.00
MINA DUMP ROAD	1/5/2021	-15.05	-118.40
MINA DUMP ROAD	2/5/2021	-15.08	-118.50
MINA DUMP ROAD	3/7/2021	-15.07	-118.50
MINA DUMP ROAD	4/3/2021	-14.91	-117.70
MINA DUMP ROAD	5/13/2021	-15.01	-118.10
MINA DUMP ROAD	6/12/2021	-14.98	-118.00
MINA DUMP ROAD	7/11/2021	-14.96	-117.90
FISH LAKE VLY HOT WELL	5/16/2020	-15.70	-126.90
FISH LAKE VLY HOT WELL	5/22/2020	-15.79	-127.50
FISH LAKE VLY HOT WELL	5/29/2020	-15.61	-127.00
FISH LAKE VLY HOT WELL	6/5/2020	-15.73	-127.40
FISH LAKE VLY HOT WELL	6/13/2020	-15.72	-127.30
FISH LAKE VLY HOT WELL	6/20/2020	-15.69	-127.20
FISH LAKE VLY HOT WELL	6/27/2020	-15.78	-127.60
FISH LAKE VLY HOT WELL	7/11/2020	-15.63	-126.90
FISH LAKE VLY HOT WELL	7/26/2020	-15.69	-127.00

FISH LAKE VLY HOT WELL	8/7/2020	-15.68	-127.10
FISH LAKE VLY HOT WELL	8/30/2020	-15.75	-127.20
FISH LAKE VLY HOT WELL	9/20/2020	-15.58	-126.90
FISH LAKE VLY HOT WELL	10/11/2020	-15.58	-126.90
FISH LAKE VLY HOT WELL	10/30/2020	-15.76	-127.30
FISH LAKE VLY HOT WELL	11/14/2020	-15.76	-127.50
FISH LAKE VLY HOT WELL	11/22/2020	-15.75	-127.30
FISH LAKE VLY HOT WELL	11/29/2020	-15.57	-127.00
FISH LAKE VLY HOT WELL	12/5/2020	-15.78	-127.60
FISH LAKE VLY HOT WELL	12/18/2020	-15.69	-127.10
FISH LAKE VLY HOT WELL	1/5/2021	-15.76	-127.50
FISH LAKE VLY HOT WELL	2/5/2021	-15.63	-127.20
FISH LAKE VLY HOT WELL	3/7/2021	-15.81	-127.60
FISH LAKE VLY HOT WELL	4/3/2021	-15.72	-127.30
FISH LAKE VLY HOT WELL	5/13/2021	-15.66	-126.90
FISH LAKE VLY HOT WELL	6/12/2021	-15.61	-126.50
FISH LAKE VLY HOT WELL	7/11/2021	-15.63	-126.90
FISH LAKE VLY HOT WELL	10/8/2021	-15.66	-126.90
COLUMBUS MARSH DEPOT	5/22/2020	-15.77	-129.80
COLUMBUS MARSH DEPOT	5/29/2020	-15.52	-129.30
COLUMBUS MARSH DEPOT	6/5/2020	-15.44	-128.90
COLUMBUS MARSH DEPOT	6/13/2020	-15.46	-129.10
COLUMBUS MARSH DEPOT	6/20/2020	-15.50	-129.40
COLUMBUS MARSH DEPOT	6/27/2020	-15.65	-129.80
COLUMBUS MARSH DEPOT	7/11/2020	-15.58	-128.90
COLUMBUS MARSH DEPOT	7/26/2020	-15.49	-128.40
COLUMBUS MARSH DEPOT	8/7/2020	-15.47	-128.70
COLUMBUS MARSH DEPOT	8/30/2020	-15.48	-128.70
COLUMBUS MARSH DEPOT	9/20/2020	-15.41	-128.60
COLUMBUS MARSH DEPOT	10/11/2020	-15.41	-128.60
COLUMBUS MARSH DEPOT	10/30/2020	-15.53	-129.00
COLUMBUS MARSH DEPOT	11/14/2020	-15.47	-128.80
COLUMBUS MARSH DEPOT	11/22/2020	-15.57	-129.10
COLUMBUS MARSH DEPOT	11/29/2020	-15.47	-128.40
COLUMBUS MARSH DEPOT	12/5/2020	-15.50	-129.10
COLUMBUS MARSH DEPOT	12/18/2020	-15.48	-128.60
COLUMBUS MARSH DEPOT	1/5/2021	-15.40	-128.70
COLUMBUS MARSH DEPOT	2/5/2021	-15.46	-128.90

COLUMBUS MARSH DEPOT	3/7/2021	-15.45	-129.00
COLUMBUS MARSH DEPOT	4/3/2021	-15.48	-129.00
COLUMBUS MARSH DEPOT	5/13/2021	-15.44	-128.70
COLUMBUS MARSH DEPOT	6/12/2021	-15.51	-128.80
COLUMBUS MARSH DEPOT	7/11/2021	-15.51	-129.00
COLUMBUS MARSH DEPOT	10/8/2021	-15.48	-128.80
WILLOW ROAD RANCH	6/20/2020	-17.44	-130.60
WILLOW ROAD RANCH	6/27/2020	-17.38	-130.20
WILLOW ROAD RANCH	7/11/2020	-17.26	-129.40
WILLOW ROAD RANCH	7/26/2020	-17.39	-129.80
WILLOW ROAD RANCH	8/7/2020	-17.27	-129.70
WILLOW ROAD RANCH	8/30/2020	-17.40	-130.00
WILLOW ROAD RANCH	9/20/2020	-17.26	-129.70
WILLOW ROAD RANCH	10/11/2020	-17.30	-129.80
WILLOW ROAD RANCH	10/30/2020	-17.37	-129.80
WILLOW ROAD RANCH	11/14/2020	-17.36	-129.90
WILLOW ROAD RANCH	11/22/2020	-17.27	-129.60
WILLOW ROAD RANCH	11/29/2020	-17.40	-130.10
WILLOW ROAD RANCH	12/5/2020	-17.36	-130.00
WILLOW ROAD RANCH	12/18/2020	-17.36	-130.00
WILLOW ROAD RANCH	1/5/2021	-17.40	-130.00
WILLOW ROAD RANCH	2/5/2021	-17.41	-130.30
WILLOW ROAD RANCH	3/7/2021	-17.47	-130.50
WILLOW ROAD RANCH	4/3/2021	-17.23	-129.80
WILLOW ROAD RANCH	5/13/2021	-17.36	-130.10
WILLOW ROAD RANCH	7/11/2021	-17.30	-130.00
WILLOW ROAD RANCH	10/8/2021	-17.33	-130.10

Appendix 7- Groundwater Isotopes $\delta^{2}H$ and $\delta^{18}O$ listed by site.